Higher sediment redistribution rates related to burrowing animals than previously assumed as revealed by Time-Of-Flight based monitoring

Paulina Grigusova[1], Annegret Larsen[2], Sebastian Achilles[1], Roland Brandl[3], Camilo del Río[4,5], Nina Farwig[6], Diana Kraus[6], Leandro Paulino[7], Patricio Pliscoff[4,8,9], Kirstin Übernickel[10], Jörg Bendix[1]

[1] Laboratory for Climatology and Remote Sensing, Department of Geography, University of Marburg, 35037 Marburg, Germany; paulina.grigusova@staff.uni-marburg.de (P.G.); bendix@geo.uni-marburg.de (J.B.)

[2] Soil Geography and Landscape, Department of Environmental Sciences, Wageningen University & Research, 6700 AA Wageningen, The Netherlands; annegret.larsen@wur.nl

[3] Animal Ecology, Department of Biology, University of Marburg, 35032 Marburg, Germany; brandlr@biologie.uni-marburg.de

[4] Facultad de Historia, Geografía y Ciencia Política, Instituto de Geografía, Pontificia Universidad Católica de Chile, 782-0436 Santiago, Chile; pliscoff@uc.cl; cdelriol@uc.cl

[5] Centro UC Desierto de Atacama, Pontificia Universidad Católica de Chile, 782-0436 Santiago, Chile; cdelriol@uc.cl

[6] Conservation Ecology, Department of Biology, University of Marburg, 35047 Marburg, Germany; diana.kraus@biologie.uni-marburg.de (D.K.); nina.farwig@biologie.uni-marburg.de (N.F.)

[7] Facultad de Agronomía, Universidad de Concepción, 3780000 Chillán, Chile; lpaulino@udec.cl

[8] Facultad de Ciencias Biológicas, Departamento de Ecología, Pontificia Universidad Católica de Chile, 8331150 Santiago, Chile; pliscoff@uc.cl

[9] Center of Applied Ecology and Sustainability (CAPES), Pontificia Universidad Católica de Chile, 8331150 Santiago, Chile; pliscoff@uc.cl

[10] Earth System Dynamics, Department of Geosciences, University of Tübingen, 72076 Tübingen, Germany; kirstin.uebernickel@uni-tuebingen.de

Corresponding author:
Paulina Grigusova
paulina.grigusova@staff.uni-marburg.de

Abstract

Burrowing animals influence surface microtopography and hillslope sediment redistribution, but changes often remain undetected due to a lack of automated high resolution field monitoring techniques. In this study, we present a new approach to quantify microtopographic variations and surface changes caused by burrowing animals and rainfall-driven erosional processes applied to remote field plots in arid and Mediterranean Chile. We compared the mass balance of redistributed sediment between burrow and burrow embedding area, quantified the cumulative sediment redistribution caused by animals and rainfall, and upscaled the results to a hillslope scale. The newly developed instrument, a Time-of-Flight camera, showed a very good detection accuracy. The animal-caused cumulative sediment excavation was 14.6 $cm^3 cm^{-2} year^{-1}$ in the Mediterranean, and 16.4 $cm^3 cm^{-2} year^{-1}$ in the arid climate zone. The rainfall-caused cumulative sediment erosion within burrows was higher (10.4 $cm^3 cm^{-2} year^{-1}$) in the Mediterranean than the arid climate zone (1.4 $cm^3 cm^{-2} year^{-1}$). Daily sediment redistribution during rainfall within burrow areas were up to 350% / 40% higher in the mediterranean / arid zone compared to burrow embedding areas, and much higher than previously reported in studies which were not based on continuous microtopographic monitoring. 38% of the sediment eroding from burrows accumulated within the burrow entrance while 62% was incorporated into hillslope sediment flux, which exceeds previous estimations two-fold. Animals burrowed between on average 1.2 – 2.3 times a month, and the burrowing intensity increased after rainfall. This revealed a newly detected feedback mechanism between rainfall, erosion, and animal burrowing activity, likely leading to an underestimation of animal-triggered hillslope sediment flux in wetter climates. Our findings hence show that the rate of sediment redistribution due to animal burrowing is climate dependant, and that animal burrowing plays a larger than previously expected role in hillslope sediment redistribution. Subsequently, animal burrowing activity should be incorporated into soil erosion and landscape evolution models that rely on soil processes but do not yet include animal-induced surface processes on microtopographical scales in their algorithms.

Keywords: Biogeomorphology, bioturbation, sediment transport, burrowing animals, rainfall, Time-of-Flight camera, Chile

81

82

83

84

85

86   **Graphical abstract**
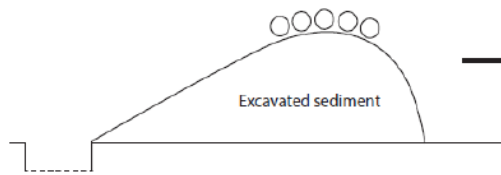
Animal-rainfall feedbacks

Arid (PdA)

(a) Initial surface
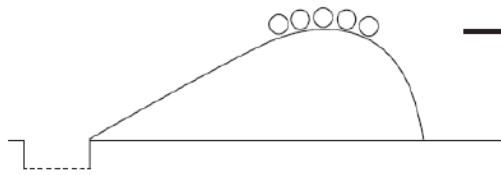
Excavated sediment
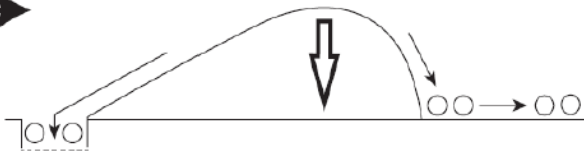
(b) Effect of animal burrowing
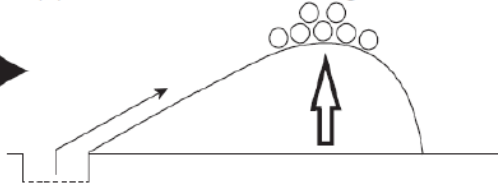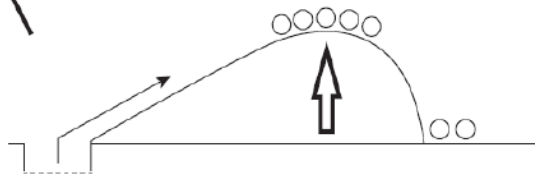
Mediterranean (LC)

(c) Initial surface

(d) Rainfall driven sediment redistribution

(e) Sediment redistribution and lower soil resistance triggers burrowing activity

87

88

1. Introduction

Animal burrowing activity affects surface microtopography (Reichman und Seabloom 2002; Kinlaw und Grasmueck 2012), surface roughness (Yair 1995; Jones et al. 2010; Hancock und Lowry 2021), and soil physical properties (Ridd 1996; Yair 1995; Hall et al. 1999; Reichman und Seabloom 2002; Hancock und Lowry 2021; Coombes 2016; Larsen et al. 2021; Corenblit et al. 2021). Previous studies estimated both positive as well as negative impacts of burrowing animals on sediment redistribution rates. These studies relied on applying tests under laboratory conditions using rainfall simulators, conducting several field campaigns weeks to months apart, or by measuring the volume of excavated or eroded sediment in the field using instruments such as erosion pins, splash boards, or simple rulers (Imeson und Kwaad 1976; Reichman und Seabloom 2002; Wei et al. 2007; Le Hir et al. 2007; Li et al. 2018; Li et al. 2019b; Li et al. 2019c; Voiculescu et al. 2019; Chen et al. 2021; Übernickel et al. 2021b; Li et al. 2019a). Although burrowing animals are generally seen as ecosystem engineers (Gabet et al. 2003; Wilkinson et al. 2009), their role in soil erosion in general, and for numerical soil erosion models in particular, is to date limited to predictions of burrow locations and particle mixing (Black und Montgomery 1991; Meysman et al. 2003; Yoo et al. 2005; Schiffers et al. 2011). The complex interaction of sediment excavation and accumulation, and erosion processes at the burrow and hillslope scale are not yet included in earth-surface-models.

The reason for this knowledge gap is that previous studies have not provided data on low magnitude but frequently occurring sediment redistribution due to a lack of spatio-temporal high-resolution microtopographic surface monitoring techniques which can also measure continuously in the field. Field experiments with, for example, rainfall simulators can unveil processes but cannot cover the time-dependant natural dynamics of sediment redistribution. When using erosion pins or splash boards, the sites had to be revisited each time and the data were thus obtained only sporadically (Imeson und Kwaad 1976; Hazelhoff et al. 1981; Richards und Humphreys 2010). This limited all previous studies in their explanatory power, because biotic-driven processes are typically characterised by small quantity and a frequent re-occurrence (Larsen et al. 2021). It is hence likely that previous studies based on non-continuously conducted measurements or rainfall experiments underestimated the role of burrowing animals on rates of hillslope sediment flux.

High-resolution, ground-based imaging sensing techniques have the potential to overcome limitations of previous surface monitoring techniques. Terrestrial laser scanner systems have been shown to be a suitable tool for the estimation of sediment redistribution and erosion processes (Nasermoaddeli und Pasche 2008; Afana et al. 2010; Eltner et al. 2016a; Eltner et al. 2016b; Longoni et al. 2016). However, these instruments are expensive and labour-intensive. Hence, a simultaneous, continuous, and automated monitoring of several animal burrows is for this reason not possible. Time-lapse photogrammetry is a low-cost (up to 5000 USD), topographic monitoring technique, which can be applied at variable observation distances and scales (e.g. (James und Robson 2014; Galland et al. 2016; Eltner et al. 2017; Mallalieu et al. 2017; Kromer et al. 2019; Blanch et al. 2021). However, several cameras are needed to monitor the surface under various angles, which makes the field installation difficult and yields the large potential to disturb the animals and lead to behavioural changes.

Another high resolution surface monitoring technique is based on Time-of-Flight (ToF) technology. ToF-based cameras illuminate the targeted object with a light source for a known amount of time and then estimate the distance between the camera and the object by measuring the time needed for the reflected light to reach the camera sensor (Sarbolandi et al. 2018). ToF cameras exhibit lower spatial resolution and aerial coverage compared to time-lapse photogrammetry. But, the technique also has several advantages: as an

active remote sensing tool it is able to monitor surface change at night, the processing is less complex compared to photogrammetry because the distance values are immediately received in a local coordinate system, and the field installation is much smaller and less invasive. ToF offers hence a new possibility for surface monitoring, as a technique for a cost-effective, high-resolution monitoring of sediment redistribution (Eitel et al. 2011; Hänsel et al. 2016), which can be achieved by a simple installation of only one device in the field.

In this study we developed, tested and applied a cost-effective Time-of-Flight camera for automated monitoring of the rainfall and burrowing animal-driven sediment redistribution of burrows and burrow embedding areas with a high temporal (four times a day) and spatial (6 mm) resolution. For this, we equipped several plots in remote field study sites in the Chilean arid and mediterranean climate zone. The selected field sites had a variable rainfall regime and sunlight exposure, and were all affected by burrowing activity (Grigusova et al. 2021). After 7 month of field monitoring including wet and dry season, we estimated burrowing intensity and its dependence on rainfall. Then, we quantified the daily sediment redistribution within the burrow and its embedding area, which enabled us to better understand the impacts of animal burrowing activity, and rainfall, on the local sediment redistribution. This allowed us to quantify the volume of burrow sediment which was incorporated into the hillslope sediment flux. Finally, we upscaled sediment redistribution rates to the entire hillslope.

2. Study area

Our study sites were located in the Chilean Coastal Cordillera in two climate zones (Fig. 1): in the National Park Pan de Azúcar (further as Pan de Azúcar or PdA) and the National Park La Campana (further as La Campana or LC). The Las Lomitas site in PdA is located in the arid climate zone of the Atacama Desert with a precipitation rate of 12 mm year^{-1}, and it has a mean annual temperature of 16.8 °C (Übernickel et al. 2021a). Here, the vegetation cover is below 5%, and it is dominated by small desert shrubs, several species of cacti (*Eulychnia breviflora, Copiapoa atacamensis)* and biocrusts (Lehnert et al. 2018). LC is located in the mediterranean climate zone with a precipitation rate of 367 mm year^{-1} and a mean annual temperature of 14.1 °C (Übernickel et al. 2021a). LC is dominated by an evergreen sclerophyllous forest with endemic palm trees, *Jubaea chilensis*. Both research sites have a granitic rock base, and the dominating soil texture is sandy loam (Bernhard et al. 2018). In PdA, the study setup consisted of one north-facing and one south-facing hillslope. The hillslope inclinations were ~20°, and a climate station was located ~15 km from the camera sites. In LC, the setup consisted of two north-facing and one south-facing hillslopes. The hillslope inclinations were ~25°, and a climate station was located ~250 m from the south-facing hillslope (Übernickel et al. 2021a).
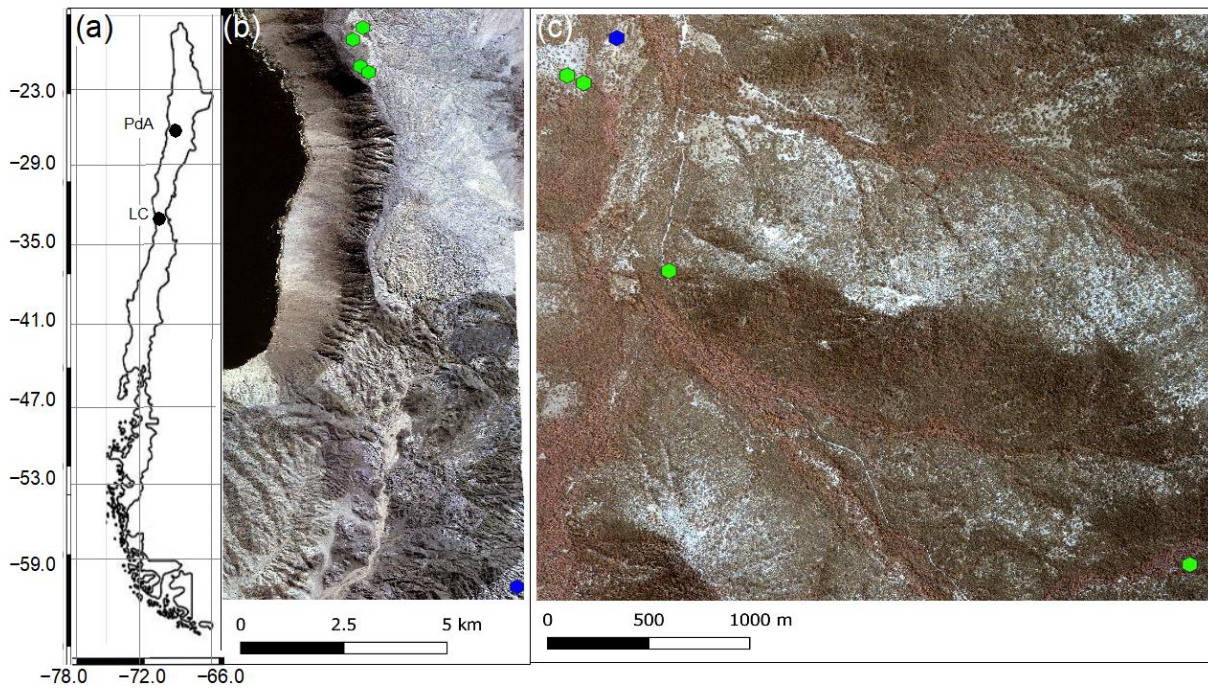
Figure 1. Location of the cameras and climate stations on which this study was based. Black points show the location of the research sites in Chile. The green points represent the camera plots, and the blue points the climate stations: (a) Location of study sites in Chile: PdA stands for Pan de Azúcar, LC for La Campana; (b) Study setup in Pan de Azúcar; (c) Study setup in LC. The background images in (b) and (c) are orthophotos created from WorldView-2 data from 19 July 2019. For exact latitude and longitude see Table A2.

2.1 Local burrowing animals

In order to assess which animal species burrowed at both study sites, we adapted a two-step approach. First, we used motion-activated camera traps to capture animals during the borrowing process at our field sites. Then, we complimented the list of identified species by a literature review. We found that the most common vertebrate animal species which burrow in PdA were carnivores of the family Canidae (*Lycalopex culpaeus*, *Lycalopex griseus*) as well as rodents of the families Abrocomidae (*Abrocoma bennetti)*, Chnichillidae (*Lagidium viscacia*), Cricetidae (*Abrothrix andinus, Phyllotis xanthopygus*, *Phyllotis limatus, Phyllotis darwini*) and Octogontidae (Cerquiera 1985, Jimenéz et al. 1992, Übernickel et al. 2021) (Table 1). In LC, the most common burrowing vertebrate animal species were the carnivores of the family Canidae, Lagomorpha of the family Leporidae (*Oryctolagus cuniculus*), and rodents of the families Cricetidae (*Abrothrix longipilis, Abrothrix olivaceus, Phyllotis darwini*), Muridae (*Mus musculus*) and Octogontidae (*Octogon degus, Spalacopus cyanus*) (Munoz-Pedreros et al. 2018, Übernickel et al. 2021) (Table 1. The motion-activated camera traps recorded several burrowing animals which all agreed with the list of burrowing vertebrate animals collected from literature: *Lycalopex culpaeus*, *Oryctolagus cunniculus* and *Abrocoma bennettii*) (Figure 2)

Table 1. Most common burrowing animals in the study sites. The list includes both, animal species recorded with our motion-activated wildlife traps and those from the review by Übernickel et al. 2021, Cerquiera 1985, Jiménez et al. 1992, Munoz-Pedreros et al. 2018). "X" indicates at which site the species can be found.

Order	Family	Species	Common name	Site	
				PdA	LC

Carnivora	Canidae	*Lycalopex culpaeus*	Culpeo	X	X
Carnivora	Canidae	*Lycalopex griseus*	South-American grey fox	X	X
Carnivora	Methitidae	*Conepatus chinga*	Molina's Hog noised skunk		X
Lagomorpha	Leporidae	*Oryctolagus cuniculus*	European rabbit		X
Rodentia	Abrocomidae	*Abrocoma bennetti*	Bennett's chinchilla rat	X	X
Rodentia	Chinchillidae	*Lagidium viscacia*	Southern mountain vischacha	X	
Rodentia	Cricetidae	*Abrothrix andinus*	Andean grass mouse	X	
Rodentia	Cricetidae	*Abrothrix longipilis*	Long-haired mouse	X	X
Rodentia	Cricetidae	*Abrothrix olivaceus*	Olive grass mouse	X	X
Rodentia	Cricetidae	*Phyllotis darwini*	Darwin's leaf-eared mouse	X	X
Rodentia	Cricetidae	*Phyllotis xanthopygus*	Yellow leaf-eared mouse	X	
Rodentia	Cricetidae	*Phyllotis limatus*	Lima leaf-eared mouse	X	
Rodentia	Muridae	*Mus musculus*	Common house mouse	X	X
Rodentia	Octogontidae	*Octogon degus*	Degu (rat)	X	X
Rodentia	Octogontidae	*Spalacopus cyanus*	Coruro (rat)	X	X

189

190

191
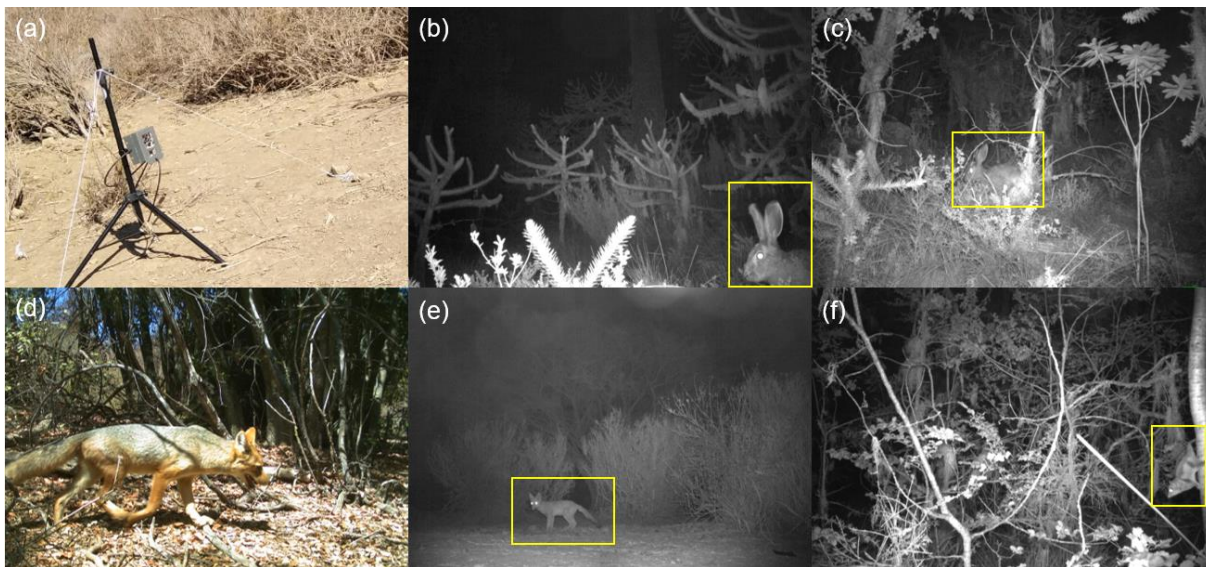
192 **Figure 2.** Examples of burrowing vertebrate animals recorded by motion-activated camera traps. (a) Set-up of
193 motion-activated camera trap. (b) and (c) European rabbit (*Oryctolagus cunniculus*). (d) and (e) Culpeo
194 (*Lycalopex culpaeus*). (f) Bennett's chinchilla rat *(Abrocoma bennettii)*. The yellow box highlights the position
195 of the animal on the photo. Photo courtesy: Diana Kraus.

196

197 **3. Methodology**

198 **3.1 Time-of-Flight (ToF) principle**

199   A Time-of-Flight-based camera illuminates an object with a light source, usually in a non-visible
200 spectrum, such as near-infrared, for a precise length of time. ToF cameras rely on the principle of measuring
201 the phase shift, with different options to modulate the light source to be able to measure the phase shift. The
202 here employed cameras used pulse-based modulation, meaning the light pulse was first emitted by the
203 camera, then reflected from the surface, and finally measured by the camera using two temporary windows.

7

204 The opening of the first window is synchronized with the pulse emission i.e. the receiver opens the window
205 with the same Δt as the emitted pulse. Then, the second window is opened, for the same duration Δt, which is
206 synchronised with the closing of the first window. The first temporary window thus measures the incoming
207 reflected light while the light pulse is also still emitting from the camera. The second temporary window
208 measures the incoming reflected light when no pulse is emitting from the camera. The captured photon number
209 (i.e. measured by electrical charge) in both windows can be related according to equation 1 and the distance
210 from the camera to the object can then be calculated as follows:

211 $$d = \frac{1}{2} * c * t * \left(\frac{g1}{g1+g2}\right) \qquad . \tag{1}$$

212 In Eq. (1), d (m) is the distance from the camera to the object, c (m s^{-1}) is the speed of light (299,792,458 m s^{-1}
213), t (s) is the overall time of the illumination and measurement, g_1 is the ratio of the reflected photons to all
214 photons accumulated in the first window, and g_2 the ratio of the reflected photons to all photons accumulated
215 in the second window (Sarbolandi et al. 2018; Li 2014).

216 The sensor in our camera came from Texas Instruments and the data scan contained information on
217 320 x 240 points. The camera field of view (FOV) and the spatial resolution of the scans depended on the
218 height of the camera above the surface and camera orientation. The distance was calculated for every point,
219 and the object was saved in binary format as a collection of 3D points with *x*-, *y*- and *z*-coordinates. The point
220 clouds taken by the camera were transformed from the binary format to an ASCII format. Each point in the
221 point cloud was assigned to an *x*-, *y*- and *z*-coordinate. The coordinates were distributed within a three-
222 dimensional Euclidian space, with the point at the camera nadir (the centre of the camera sensor) being the
223 point of origin of the 3D Cartesian coordinate system. *x*- and *y*-coordinates describe the distance to the point
224 of origin (m). *z*-coordinate describes the distance (m) from the object to the camera. The lowest point of the
225 scanned surface thus has the highest *z*-coordinate value.

226

227 **3.2 Data processing**
228 The distortion caused by the hillslope and the camera angle was corrected for each point cloud as
229 follows:

230 $$z_{cor} = z_{uncor} - \tan(\alpha + \beta) * (y_1 - y_i) \qquad . \tag{2}$$

231 In Eq. (2), z_{cor} is the corrected distance (m) between the camera and surface (m), z_{uncor} is the uncorrected *z*-
232 coordinate (m), α is the tilt angle of the camera (°), β is the surface inclination (°), and y_i (m) is the distance
233 between each point, and the point with i) an y-coordinate = 0 and ii) the same x-coordinate as the respective
234 point. The most frequent errors were identified and treated as follows. Due to the ambient light reaching the
235 camera sensor, the *z*-coordinate values of some of the points were incorrect (scattering error). To remove this
236 error, a threshold value was calculated for each point cloud:

237 $$\Omega = mean_{zcor-coordinates} \pm sd_{zcor-coordinates} \qquad . \tag{3}$$

238 In Eq. (3), Ω is the threshold value, $mean_{zcor-coordinate}$ is the average value, and $sd_{zcor-coordinate}$ is the standard
239 deviation of the corrected *z*-coordinates (m). Then, all points with a *z*-coordinate above and below this value
240 were deleted. Point clouds with more than 50% of points above the threshold value Ω were also not considered
241 for further processing. A drift error occurred when the *z*-coordinate values of around one-third of the point
242 clouds decreased by several centimetres from one point cloud to another. Here, the average *z*-coordinate of
243 ten point clouds before and after the drift were calculated, and the difference was added to *z*-coordinates of

the points affected by the drift. The corrected height values were then transformed into a digital surface model (DSM).

3.3 Accuracy of the ToF cameras

The accuracy of the ToF camera was tested under laboratory conditions by recreating similar surface conditions as in the field (sloping surface, covered by sediment). An artificial mound using sediment extracted from a riverbank in central Germany was used, mimicking a mound created by a burrowing animal. During the test, the camera was installed 100 cm above the surface. The camera FOV was 3 m^2 and the scan spatial resolution was 6 mm. The surface was scanned twice by the ToF camera. Then 100 – 450 cm^3 of sediment was manually extracted from the mound. The volume of the extracted sediment was measured by a measuring cup. After extraction, the surface was again scanned twice by the camera. The experiment was repeated 45 times with varying amounts of extracted sediment. The scans were transformed to point clouds in VoxelViewer-0.9.10, and the point clouds were corrected according to Eq. (2) and (3). The z-coordinates of the two point clouds before and two point clouds after the extraction were averaged. The standard deviation of the z-coordinate of the two scans was 0.06 cm. Figure A1 shows the spatially distributed standard deviation. The deviation increases from the centre towards the corners of the scan. The mound was outlined and only the points representing the mound were used in the further analysis. The point clouds were then transformed into DSMs, and the differences between the time steps were calculated. A scan was taken of a smooth surface (linoleum floor) and a point cloud was created from the data. Then, we fitted a plane into the point cloud and calculated the distance between the plane and the camera sensor. The standard variation (0.17 cm) in the distance measurements was saved. Solely, the differences between the DSMs below this variation were considered in the calculation of the detected sediment extraction. The detected extracted sediment volume was then calculated for each experiment as follows:

$$Vol_{detected} = \sum_p^1 (DSM_{before} - DSM_{after}) * res^2 \qquad , \qquad (4)$$

In Eq. (4), $Vol_{detected}$ is the volume of the extracted sediment as detected by the camera (cm^3), p is the number of pixels, DSM_{before} (cm) is the DSM calculated from the scan taken before the extraction, DSM_{after} (cm) is the DSM calculated from the scan taken after the extraction, res (cm) is the resolution of the scan, which was 0.6 cm. To evaluate the camera's accuracy, the measured volume of the extracted sediment was compared to the volume detected by the camera. The camera's accuracy was estimated between the detected volume and measured volume as follows:

$$MAE = \sum_1^n \frac{(Vol_{detected} - Vol_{measured})}{area} \qquad . \qquad (5)$$

In Eq. (5), MAE (cm^3/cm^2) is the mean absolute error, n is the number of scans, $Vol_{measured}$ (cm^3) is the volume of the extracted sediment measured by the measuring cup, and the area is the total surface area monitored by the camera (cm^2).

3.4 Installation of the cameras in the field

We installed 8 custom-tailored ToF-based cameras on 4 hillslopes in two climate zones in areas including visible signs of bioturbation activity (burrows) and areas without visible signs of bioturbation (Fig. 3). The cameras were installed in LC on the north-facing upper hillslope (LC-NU), north-facing lower hillslope (LC-NL), south-facing upper hillslope (LC-SU) and the south-facing lower hillslope (LC-SL); in PdA on the north-facing upper hillslope (PdA-NU), north-facing lower hillslope (PdA-NL), south-facing upper hillslope (PdA-SU)

285   and south-facing lower hillslope (PdA-SL). The custom-tailored cameras were installed during a field campaign
286   in March 2019, the monitoring took place for seven months, and the data were collected in October 2019. The
287   construction consisted of a 3D ToF-based sensor from Texas Instruments (Li, 2014), a RasperryPi single board
288   computer (SBC), a timer, a 12 V 12 Ah battery and three 20 W solar panels for unattended operation (Fig. 2).
289   Solar panels were located at the camera pole and were recharging the battery via a charge controller. The
290   camera was located approximately one meter above the surface, facing the surface with a tilt angle of 10
291   degrees. The timer was set to close the electric circuit 4 times a day: at 1 a.m., 5 a.m., 8 a.m. and 10 p.m. At
292   these times, the camera and the computer were turned on for 15 minutes. The camera turned on and took five
293   scans delayed one second from each other and sent them to the SBC. Each camera had its own WiFi (Wireless
294   Fidelity) and the data could be read from the SBC via Secure Shell (SSH). The cameras collected the data for
295   the time period of 7 months.
296
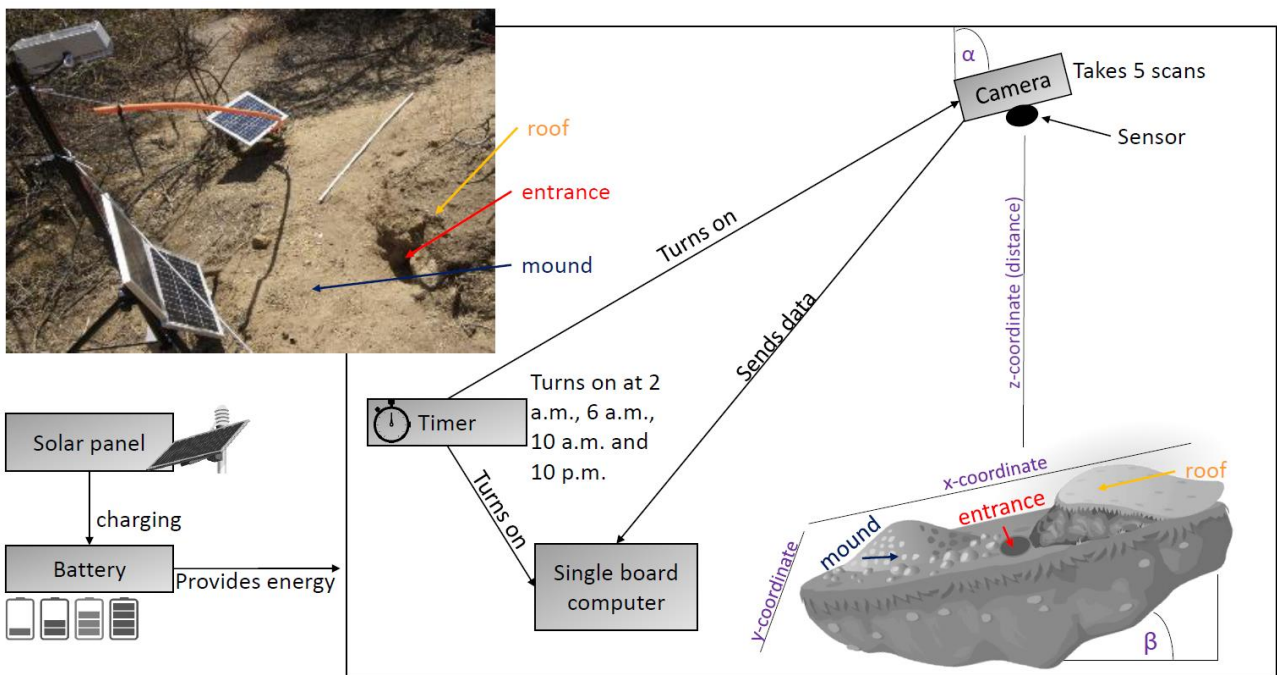
298   **Figure 3.** Scheme and photo example of a Time-of-Flight-based camera installation in the field. The photo
299   example is from upper north-facing hillslope in La Campana. Black boxes describe single installation parts.
300   Purple descriptions are the variables needed for the correction of the scans. Roof, entrance and mound
301   describe parts of the burrow. The x-, y- and z-coordinates are 3D coordinates identifying the position of each
302   point in space, where the x-coordinate is the length, y-coordinate is the width and the z-coordinate is the
303   distance between the camera sensor and the surface. α is the inclination of the camera, and β is the surface
304   inclination.
305

## 3.5 Delineation of burrows and burrow embedding areas

307   The surface area scanned by the cameras was divided by a delineation scheme into burrows (B) and
308   burrow embedding areas (EM). The burrows included three sub-areas: (i) mound (M), (ii) entrance (E) and (iii)
309   burrow roof (R). "Mound" describes the sediment excavated by the animal while digging the burrow. "Entrance"
310   describes the entry to the animal burrow up to the depth possible to obtain via the camera. "Burrow roof"
311   describes the part of the sediment above and uphill the burrow entrance (Bancroft et al. 2004). During the
312   burrow's creation, sediment was not only excavated but also pushed aside and uphill the entrance, which

313 created the burrow roof. We assume that this elevated microtopographical feature then forms an obstacle for
314 sediment transported from uphill, which leads to its accumulation in this area. The remaining surface within
315 the camera's FOV was burrow embedding area. Please note, that this area may still be affected by the
316 burrowing activity of the animal and is not completely unaffected by the animal.

317   For the delineation, we used the DSM calculated from the point cloud, and a slope layer calculated
318 from the DSM (Horn 1981). The DSM had a size of 4 m^2 a resolution of 0.6 cm. Entrance was assigned to an
319 area determined by a search algorithm starting at the lowest point of the DSM (pixel with the highest z-
320 coordinate value). We increased the circular buffer around the starting point by one pixel until the average
321 depth of the new buffer points was not higher than the height of the camera above the surface, or until the
322 slope of at least 50% of the new buffer points was not 0. Then, we masked all pixels within the buffer with a
323 depth lower than the average depth of the points within the buffer, which had a slope that was 0. The remaining
324 pixels belonged to the entrance area. Then, the surface scan was divided into an uphill and downhill part with
325 regards to the entrance position. Both the uphill and the downhill parts were subdivided into 16 squares, so
326 that each of the four quadrants within the 2D grid (x- and y-axis) contained four squares. The squares had size
327 of 0.5 m^2.

328 To delineate the mound in the downhill part, we first identified the highest points (pixel with the lowest z-
329 coordinate value) within all 16 squares. We then calculated the distance of these maxima to the entrance, and
330 the pixel located nearest to the entrance was identified as the highest point of the mound (i.e., seed point).
331 Consecutively, we increased the circular buffer around the seed point by one pixel until the average depth of
332 the new buffer points was not lower than the height of the camera above the surface, or until the slope of at
333 least 50% of the new buffer points was not 0. Then, we masked all pixels within the buffer with a depth higher
334 than the average depth of the points within the buffer, which had a slope that was 0. The remaining pixels were
335 classified as mound area. To delineate burrow roof, we used the same approach as for the delineation of
336 mound and applied it on the uphill part of the surface scan. We used the DEM and slope layers for the
337 delineation for several reasons. The distance from the surface to the camera was the most important parameter
338 to derive (i) the deepest point of the entrance and (ii) the highest point of the mound or burrow roof, as this
339 was (mostly) the closest point to the camera. After the angle correction of the z-coordinate according to chapter
340 3.2., the surface inclination of the areas without burrow was 0°, while the angle between the border of the
341 burrow entrance or mound and the burrow embedding surface was above 0°. Because neither the entrance
342 nor the mound have a perfect circular form, we would largely overestimate or underestimate the entrance or
343 mound size. Overestimate by not stopping the search algorithm until the angle between all new points of the
344 buffer to the rest of the buffer was 0°. Underestimate by stopping the algorithm when the angle of one point of
345 the buffer to the nearest point of the buffer was 0°. The value of 50% thus minimized the error. All pixels that
346 were not classified during the entire delineation process were treated as burrow embedding areas.
347 The position and the boundaries of entrance, mound and burrow roof were validated visually (Fig. 4 and A2).
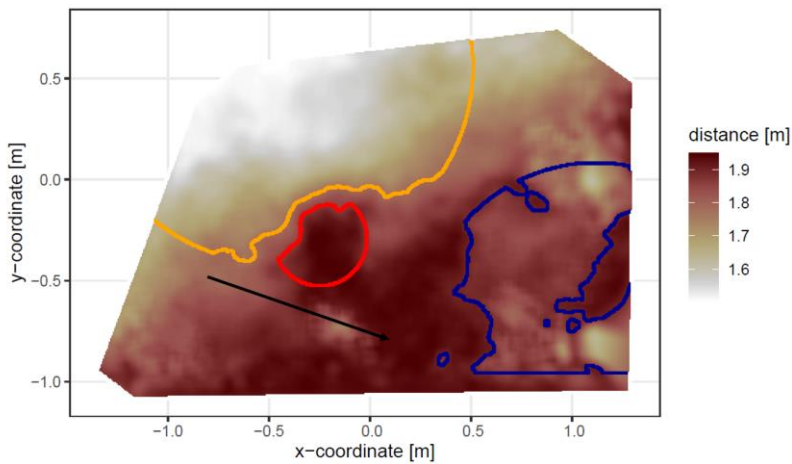
Figure 4. Corrected digital surface model of the camera on the upper north-facing hillslope in La Campana with delineated areas. The point of origin of the coordinate system is at the camera nadir. Distance refers to the distance between surface and camera. The red line delineates the burrow entrance, blue the mound and orange the burrow roof. The area which was outside of any delineated area was classified as burrow embedding area. The arrow indicates a downhill direction of the hillslope.

In LC, the burrows always consisted of an entrance, mound and burrow roof. In PdA, there was no burrow roof on the upper hillslopes. Burrows without a burrow roof were located on shallower parts of the hillslopes (up to an inclination of 5°), and the angle of the burrow entrance to the ground was ~90°. Burrows with a burrow roof were located on steeper parts of the hillslopes (with an inclination above 5°), and the angle of the burrow entrance to the ground was ~45°.

3.6 Calculation of animal-caused and rainfall-caused sediment redistribution

We pairwise compared the DSMs of each scan with the scan saved before and identified 3 types of sediment redistribution which occurred in the time period between these images. The 3 types of redistribution were: a) animal caused; b) rainfall-caused; c) both animal and rainfall caused.

The animal-caused sediment redistribution occurred when the animal actively reworked sediment within its burrow. Following five prerequisites had to be met when the sediment redistribution was caused solely by the animal: (i) as the animal excavates sediment from the entrance, the depth of the entrance must increase in the second scan; (ii) as the excavated sediment accumulates on the mound, the height of the mound must increase in the second scan; (iii) as the burrowing might lead to an expansion or a collapse of the burrow roof, an increase or decrease of the burrow roof must occur between the scans; (iv) as the animal only digs within his burrow, no changes must occur between the two scans within the burrow embedding area by the animal; (v) no rainfall occurred during this period.

The rainfall-caused sediment redistribution was calculated as follows: From the data from the climate stations (Übernickel et al. 2021a), we calculated the daily precipitation in mm. The sediment redistribution recorded immediately and within five scans before and after a rainfall event is defined to be the result of the rainfall event. This was necessary as the climate stations are located up to a 15 km distance from the cameras (Fig. 1). To attribute sediment redistribution to rainfall event, three preconditions had to be met: (i) A rainfall event occurred; (ii) sediment is eroded from burrow roof, mound and the embedding area; (iii) sediment is accumulated within the burrow entrance.

380   To attribute sediment redistribution to a combination of animal activity and rainfall, four preconditions
381 had to be met: (i) A rainfall event occurred; (ii) sediment is eroded from embedding area; (iii) the height of
382 burrow roof and mound decreased or increased; (iv) the depth of burrow entrance increased.

383   The animal-caused sediment redistribution was calculated as the sediment volume excavated from
384 the entrance. Animal excavation always increased depth of the burrow entrance. The rainfall-caused sediment
385 redistribution was calculated as the sediment volume which eroded from the burrow roof and mound. During
386 a rainfall event, sediment eroding from burrow roof might accumulate within burrow entrances. In this case,
387 the depth of the burrow entrance decreased. No sediment could erode from the entrance during a rainfall
388 event. Decreased depth of a burrow entrance always points to sediment redistribution caused by rainfall,
389 increased depth of burrow entrance always means redistribution by animals. Rainfall-caused redistribution
390 always occurred before animal-caused redistribution, as without erosion caused by rainfall, the animals did not
391 need to reconstruct their burrows.

392

393 **3.7 Calculation of daily sediment mass balance budget**

394   The volume of the redistributed sediment was calculated daily and was then cumulated from the first
395 day of monitoring. For the calculation of the daily sediment redistribution, the change in the surface level
396 detected by the camera was calculated first. For each day, the scans from the day before and after the
397 respective day were averaged and subtracted. The average standard deviation of the z-coordinate of these
398 scans was 0.06 cm. As described in Section 2.2., all values with a difference below and above the threshold
399 value of 0.2 cm were set to 0. The redistributed sediment volume was then calculated from the surface change
400 for each pixel as follows:

401 $$Vol_{redistributed} = (S_b - S_a) * res^2 \qquad .$$ (6)

402 In Eq. (6), $Vol_{redistributed}$ (cm^3 pixel^{-1}) is the volume of the calculated redistributed sediment, S_b (cm) the scan
403 before, S_a (cm) the scan after the rainfall event and *res* is the spatial resolution (cm). Using the daily volume
404 of the redistributed sediment per pixel, we calculated the daily mass balance budget by summing the volume
405 of sediment eroding or accumulating within each delineated area.

406

407 **3.8 Calculation of the overall volume of redistributed sediment after the period of 7 months**

408   From the camera data, we calculated the average cumulative volume of redistributed sediment for the
409 period of 7 months within burrows ($Vol_{burrows}$ (cm^3 cm^{-2} year^{-1})) and burrow embedding ($Vol_{embedding}$ (cm^3 cm^{-2}
410 year^{-1})) areas and the average sediment volume redistributed (excavated) by the animal (Vol_{exc} (cm^3 cm^{-2}
411 year^{-1})), separately for each site. We estimated the volume of sediment that was redistributed during rainfall
412 events due to the presence of the burrow (Vol_{add} (cm^3 cm^{-2} year^{-1})). Vol_{add} was calculated as the difference in
413 the redistributed sediment volume between burrows and burrow embedding areas according to Eq. (7).

414 $$Vol_{add} = (Vol_{affected} - Vol_{unaffected}) * 1.71 \qquad ,$$ (7)

415 Additionally, we calculated the average volume of the redistributed sediment per burrow ($Vol_{per\ burrow}$ [cm^3
416 burrow^{-1} year^{-1}]).

417 $$Vol_{per\ burrow} = (Area_{burrow} * Vol) * 1.71$$ (8)

418 In Eq. (8), $Area_{burrow}$ (cm^2) is the average size of the burrows that are monitored by the cameras; Vol is Vol_{burrow}
419 (cm^3 cm^{-2} year^{-1}), Vol_{exc} (cm^3 cm^{-2} year^{-1}) or Vol_{add} (cm^3 cm^{-2} year^{-1}).

420   We then upscaled the Vol_{burrow} (cm^3 cm^{-2} year^{-1}), Vol_{exc} (cm^3 cm^{-2} year^{-1})) and Vol_{add} (cm^3 cm^{-2} year^{-1})) to the hillslope using the following approach. Hillslope-wide upscaling of the results generated in this study

was performed by using a previous estimation of vertebrate burrow density (Grigusova et al. 2021). In this study, the density of burrows was measured in situ within eighty 100 m^2 plots and then upscaled to the same hillslopes on which the cameras were located by applying machine-learning methods, using the UAV-data as predictors. For upscaling, we applied a random forest model with recursive feature elimination. The model was validated by a repeated Leave-One-Out cross validation. The density of vertebrate burrows was between 6 and 12 100 m^2 in LC and between 0 and 12 100 m^{-2} in Pan de Azúcar. Using the hillslope-wide predicted vertebrate burrow densities (Dens$_{burrow}$ (number of burrows 100 m^{-2})) from Grigusova et al. 2021, we estimated the volume of redistributed sediment for each pixel of the raster layers (Vol$_{per pixel}$ (cm^3 m^{-2} year^{-1})) according to Eq. (9):

$$Vol_{per\ pixel} = Vol_{per\ burrow} * Dens_{burrow} * 1.71 \qquad\qquad (9)$$

The average hillslope-wide volume of redistributed sediment (Vol$_{hillslope-wide}$ (m^3 ha^{-1} year^{-1})) was then estimated as follows:

$$Vol_{hillslope-wide} = \sum_1^m Vol_{per\ pixel} * 0.001 * 1.71 \qquad\qquad , \qquad\qquad (10)$$

In Eq (10), m is the number of pixels.

4. Results

4.1 Camera accuracy and data availability

The accuracy between the measured extracted sediment volume and sediment volume calculated from the camera scans was very high (MAE = 0.023 cm^3 cm^{-2}, R^2 = 0.77, SD = 0.02 cm^3 cm^{-2}, Fig. A3). The accuracy between the calculated and measured extracted sediment was higher when the two scans taken before as well as after the extraction of the sediment were averaged and the sediment volume was estimated using these averaged scans. When calculating the redistributed sediment from solely one scan before and after extraction, the accuracy slightly decreased (MAE = 0.081 cm^3 cm^{-2}, R^2 = 0.64). The cameras tended to overestimate the volume of redistributed sediment. Six out of eight custom-tailored cameras collected data over the seven-month period (Table A2). One camera collected data for a period of three months and one camera stopped working a few days after installation. The quantity of usable point clouds taken at 1 a.m., 5 a.m. and 10 p.m. was higher than of point clouds taken at 8 a.m. Approximately 20% of points was removed from the point clouds before final analysis due to the high scattering at the point cloud corners. After data filtering (see Section 3.2.), 1326 scans were usable and for 86% of the days, at least one usable scan was available. The usable scans were distributed continuously within the monitoring period.
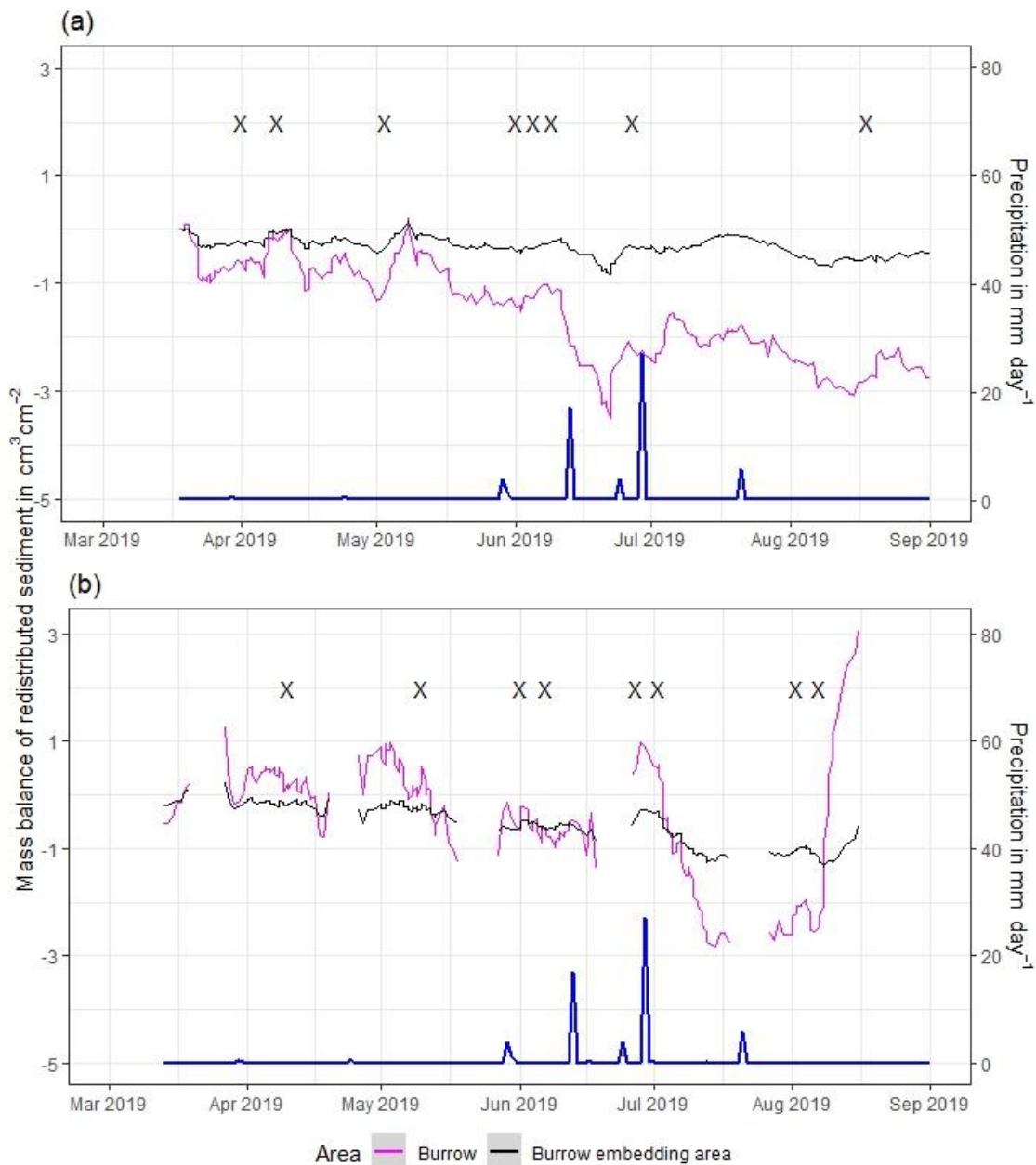
4.3 Mass balance of redistributed sediment

The cameras detected (i) sediment redistribution directly following rainfall events and (ii) due to the burrowing activity in times without rainfall (Fig. 5, A4 and A5). In all cases, burrows (entrance, burrow roof and mound) exhibited higher sediment redistribution rates than burrow embedding areas. In addition, the volume of redistributed sediment by animal activity was higher after a rainfall event occurred.

In the following, the dynamics are exemplary explained for four cameras. Animal burrowing activity was detected seven times by the camera LC NU (Fig. 5a, A4, A5) during the monitoring period, by an increase in sediment volume in the area delineated as mound. Simultaneously, the burrow entrance showed signs of modification and sediment accumulation, but these changes were less clear. Overall, the volume of the excavated soil varied. From April until June, up to 0.5 cm^3 cm^{-2} of sediment was excavated by the animal and accumulated on the mound. From June until September, animal burrowing activity was detected at four time

464 slots (5 June 2019, 9 June 2019, 1 July 2019 and 18 August 2019) and sediment volume of up to 2 cm^3 cm^{-2}

465 accumulated each time on the mound, burrow roof and within the entrance. During the rainfall events of up to

466 20 mm day^{-1} on 16 June 2019, 27 mm day^{-1} on 29 June 2019 and 7 mm day^{-1} on 13 July 2019, sediment

467 volume of up to 4 cm^3 cm^{-2} eroded, especially from the burrow roof and the mound while a sediment volume

468 of up to 1 cm^3 cm^{-2} accumulated within the entrance during each rainfall event. Camera LC-SL (Fig. A4, A5)

469 showed burrowing activities eight times and sediment volumes of up to 3 cm^3 cm^{-2} accumulated within the

470 entrance and burrow roof. The camera detected sediment erosion of up to 2 cm^3 cm^{-2} after a rainfall event of

471 27 mm day^{-1} on 27 July 2019. On the south-upper hillslope, the camera detected animal burrowing activity six

472 times, with a sediment accumulation of up to 3 cm^3 cm^{-2} (Fig. A2 and A3).

473   In contrast, camera PdA-NU pointed to animal burrowing activity up to 15 times where up to 1 cm^3 cm$^-$

474 ^{2} of sediment volume was redistributed from the entrance to the mound (Fig. 5b, A4, A5). At the end of June

475 on 27 June 2019, a rainfall event of 1.5 mm day^{-1} occurred and up to 2 cm^3 cm^{-2} of sediment eroded from the

476 burrow roof and accumulated within the burrow entrance. We observed increased sediment redistribution by

477 the animal after the rainfall events. Camera PdA-SL evenly revealed animal burrowing activity up to 15 times

478 ((Fig. A4, A5)). The burrowing had a strong effect on the sediment redistribution. The rainfall event of 1.5 mm

479 day^{-1} on 27 June 2019 did not cause any detectable surface change.

Figure 5. Examples of the mass balance of redistributed sediment for burrows and burrow embedding areas (**a**) The record of the camera on the upper north-facing hillslope in La Campana showed that larger rainfall events cause a negative sediment balance (sediment loss), followed by a phase of positive sediment mass balance after approximately 3 days due to sediment excavation; (**b**) The record of the camera on the upper north-facing in Pan de Azúcar hillslope showed a similar pattern to the camera on the upper north-facing hillslope, but the phase of positive mass balance was delayed in comparison. The blue line is the daily precipitation in mm day^{-1}, and "X" marks the days at which animal burrowing activity was detected. Positive values indicate sediment accumulation. Negative values indicate sediment erosion. Mass balances for all cameras are displayed in Fig. A2 and A3.

The analysis of cumulative volume of the redistributed sediment caused by burrowing animal activity and rainfall over the monitored period of seven months for all eight cameras showed a heterogeneous pattern.

16

494   In LC, the cumulative volume of the sediment excavated by the animal within the burrow roof and
495 mound increased continuously (Fig. 6, A7). Especially between the rainfall events from June until August, a
496 cumulative volume of on average 6.5 cm^3 cm^{-2} was excavated by the animal. We calculated that, on average,
497 8.53 cm^3 cm^{-2} cumulatively eroded from the burrow roof and mound; while 2.44 cm^3 cm^{-2} sediment volume
498 accumulated within the entrance (Fig. 6, A7). These results indicate that 28% of sediment eroding from the
499 burrow roof accumulated within the entrance, while over 62% of sediment eroded downhill. Averaged over all
500 camera scans, 338% more sediment was redistributed by rain within burrow compared to the burrow
501 embedding area (Fig. 7).

502   In PdA, cameras continuously detected animal burrowing activity and excavation of the sediment (Fig.
503 A7). The volume of the detected excavated sediment increased steadily within all cameras. The cumulative
504 sediment accumulation surpasses the sediment eroded due to the rainfall. The volume of the sediment eroded
505 within the burrows was 40% higher than within the burrow embedding areas. The results show that
506 approximately 50% of the eroded sediment accumulated within the entrance (Fig. 7).

507
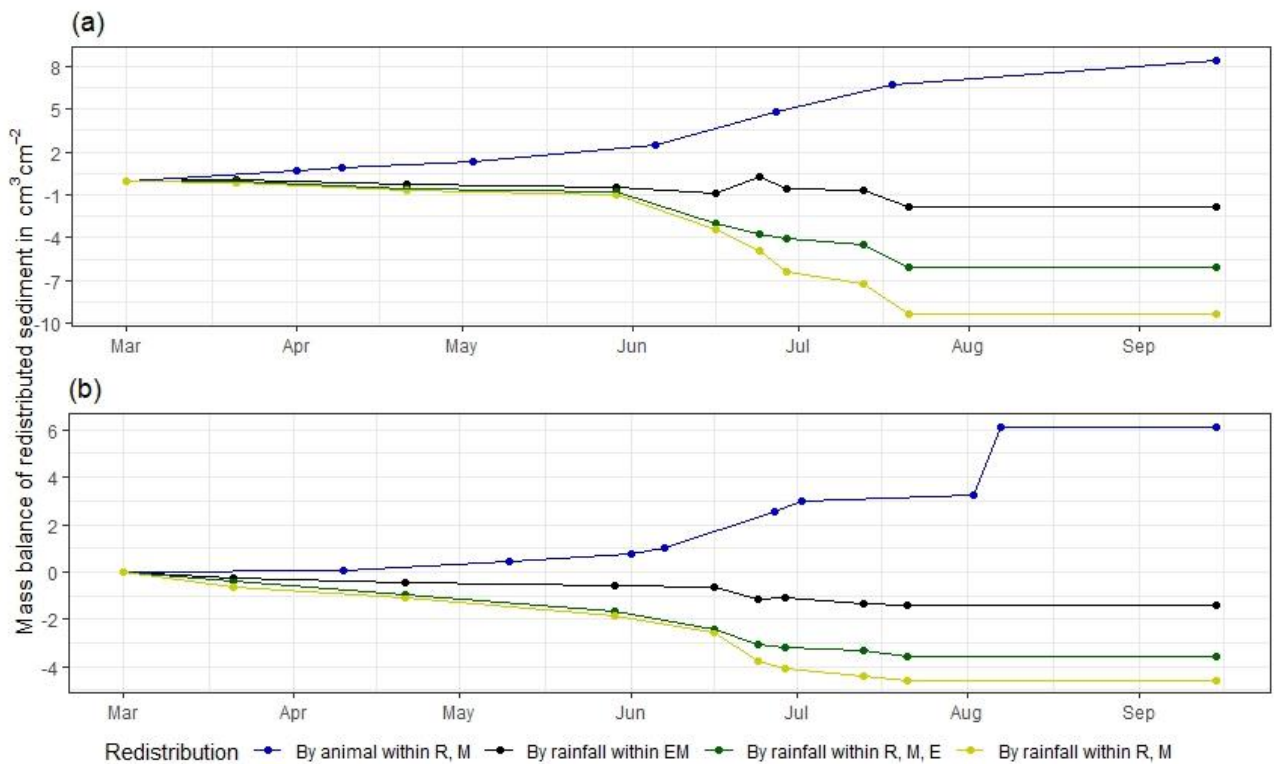
Figure 6. Examples of the cumulative volume of redistributed sediment within burrows and burrow embedding
areas caused by animal burrowing activity or rainfall in mediterranean La Campana: (a) Upper north-facing
hillslope; (b) Lower south-facing hillslope. Positive values indicate sediment accumulation. Negative values
indicate sediment erosion. E is the burrow entrance; M is the mound; R is burrow roof; EM is the burrow
embedding area. Cumulative volumes for all cameras are in Fig. A7.
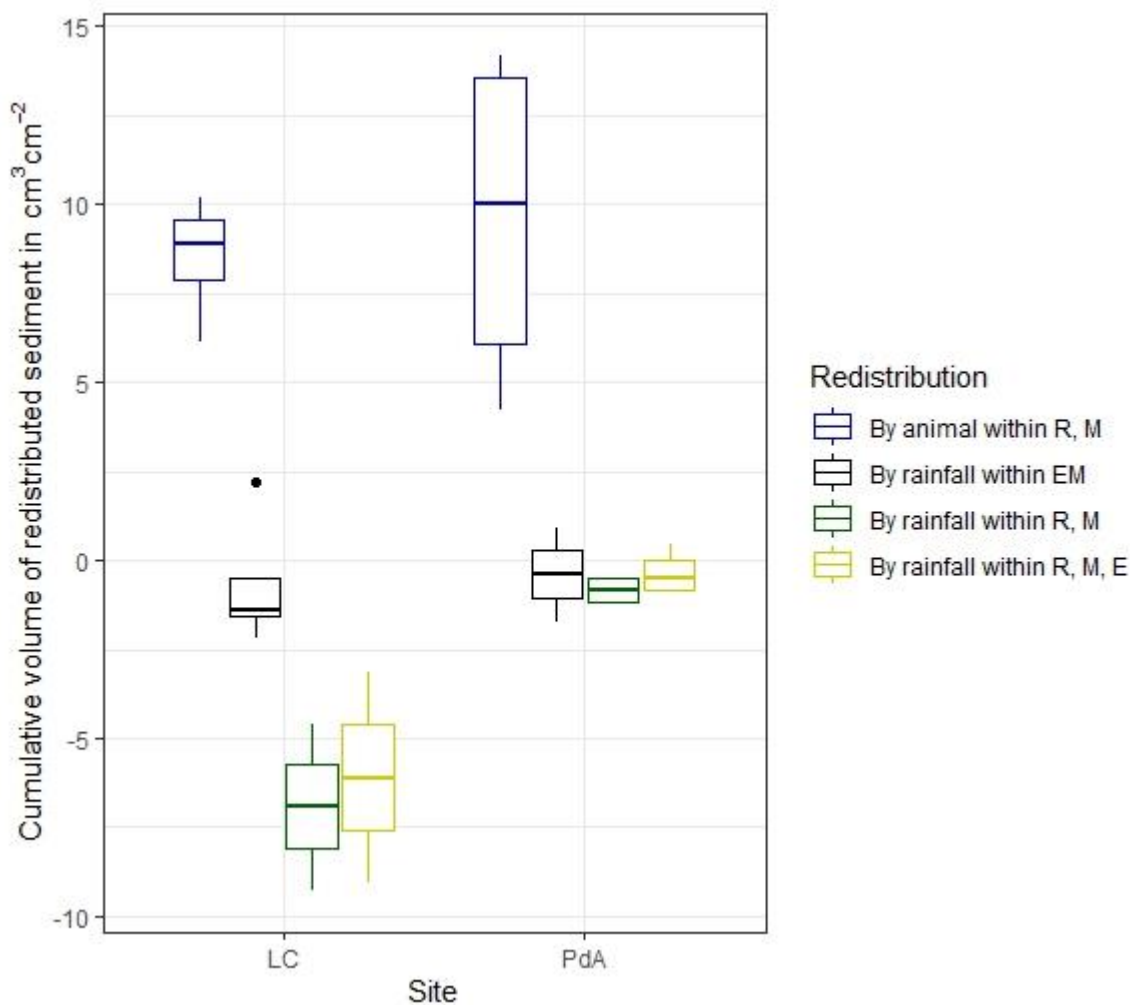
Figure 7. Cumulative volume of the redistributed sediment for the time period of 7 months for all cameras. Positive values indicate sediment accumulation. Negative values indicate sediment erosion. Whiskers indicate the median of sediment redistribution. E is the burrow entrance; M the mound; R is the burrow roof; EM is burrow embedding area; LC stands for National Park La Campana in the mediterranean climate zone; PdA stands for National Park PdA in the arid climate zone.

4.4 Volume of redistributed sediment

The average size of the burrows was 84.3 cm^2 (SD = 32.5 cm^2) in LC and 91.3 cm^2 in PdA (SD = 8.5 cm^2). The animals burrowed on average 1.2 times month^{-1} in LC and 2.3 times month^{-1} in PdA. The volume of the excavated sediment was 102.2 cm^{-3} month^{-1} in LC and 124.8 cm^3 month^{-1} in PdA. Each time the animals burrowed, they excavated 42 cm^3 sediment volume in LC and 14.3 cm^3 sediment volume in PdA. The burrowing intensity increased in winter after the rainfall occurrences in LC and stayed constant during the whole monitoring period in PdA. The burrows deteriorate after rainfall events with a rate of 73.0 cm^3 month^{-1} or 63.9 cm^3 event^{-1} in LC and 10.5 cm^{-3} month or 24.5 cm^3 event^{-1}.

The overall volume of the sediment excavated by the animal and redistributed during rainfall events varied between the sites (Table 1). The volume of the sediment redistributed by the animal was lower in LC than in PdA. However, on the hillslope scale, a higher total area-wide volume of excavation was calculated for LC compared to PdA, due to the higher burrow density in LC. The volume of the sediment redistributed within

533 burrows during rainfall events was higher in LC than in PdA. The volume of additionally redistributed sediment

534 due to the presence of burrows was higher in LC than in PdA (Table 2, Fig. 8).

535

536 **Table 2.** Summary of the volume of redistributed sediment, according to area and disturbance type. Vol_{exc}

537 describes volume of the sediment excavated by the animals. Vol_{burrow} describes volume of the sediment

538 redistributed during rainfall events within burrows. Vol_{add} describes the difference in redistributed sediment

539 volume within burrows and burrow embedding areas during rainfall. Positive values indicate sediment

540 accumulation; negative values indicate sediment erosion.

Disturbance	Area	PdA	LC
Vol_{exc}	Burrow	16.4 cm^3 cm^{-2} year^{-1}	14.6 cm^3 cm^{-2} year^{-1}
	Per burrow	1498.6 cm^3 burrow^{-1} year^{-1}	1226.1 cm^3 burrow^{-1} year^{-1}
	Hillslope-wide	0.8 m^3 ha^{-1} year^{-1}	0.7 m^3 ha^{-1} year^{-1}
$Vol_{affected}$	Burrow	-1.9 cm^3 cm^{-2} year^{-1}	-10.4 cm^3 cm^{-2} year^{-1}
	Per burrow	-126.3 cm^3 burrow^{-1} year^{-1}	-876.8 cm^3 burrow^{-1} year^{-1}
	Hillslope-wide	-0.1 m^3 ha^{-1} year^{-1}	-0.4 m^3 ha^{-1} year^{-1}
Vol_{add}	Burrow	-1.1 cm^3 cm^{-2} year^{-1}	-7.3 cm^3 cm^{-2} year^{-1}
	Per burrow	-48.3 cm^3 burrow^{-1} year^{-1}	-619.2 cm^3 burrow^{-1} year^{-1}
	Hillslope-wide	-0.1 m^3 ha^{-1} year^{-1}	-0.3 m^3 ha^{-1} year^{-1}

541
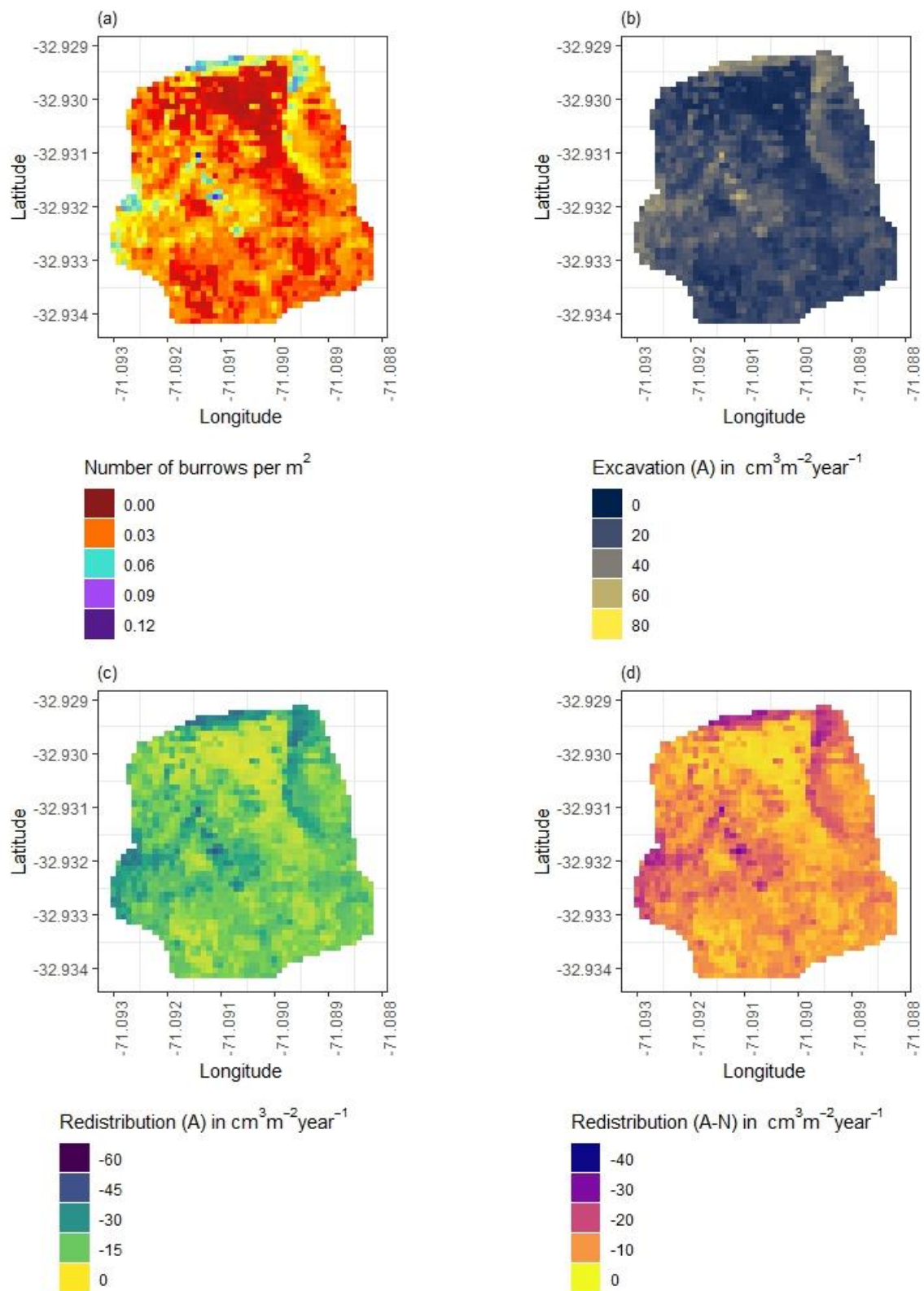
Figure 8. Example of the hillslope-wide volume of redistributed sediment on the south-facing hillslope in La Campana: (a) Density of burrows as estimated by Grigusova et al. (2021); (b) Volume of the sediment excavated by the animals; (c) Volume of the sediment redistributed during rainfall events within burrows; (d) Volume of additionally redistributed sediment during rainfall events due to the presence of the burrows. The values were calculated per burrow as stated in Section 3.7. by subtracting the sediment volume redistributed within burrows from the sediment volume redistributed within burrow embedding area and then upscaled. The letters in brackets indicate if the upscaling was conducted using data from burrows or burrow embedding areas.

"B" stands for burrow. By "EM-B", the redistribution calculated within burrow embedding areas was subtracted from the redistribution calculated within burrows to obtain the additional volume of redistributed sediment due to the burrows' presence. Positive values indicate sediment accumulation. Negative values indicate sediment erosion.

5. Discussion

Our results showed that the custom-made ToF device is a suitable tool for high-resolution, automated monitoring of surface changes, applicable also in remote areas. The continuous observation of sediment redistribution over a longer time period provided new insights into the relative importance of burrowing animals for hillslope sediment flux. Our research revealed that the presence of vertebrate burrows increases hillslope sediment redistribution rates much more than previously assumed (increase of up to 208%). We showed that the quantity of animal-related sediment redistribution, however, varied with rainfall occurrence, with an increase in sediment redistribution between 40% in the arid research area and 338% percent in the mediterranean research area.

5.1 Suitability of the ToF - cameras for surface monitoring

The newly introduced monitoring technique ToF enables an automatic monitoring of surface changes on a microtopographic scale, and is less costly and invasive than other techniques. The measurement continuity of the device also allows for the analysis of ongoing biogeomorphological processes in high temporal and spatial resolution.

With regard to the costs, measurement frequency and sampling autonomy, the custom-made ToF device constitutes an improvement to earlier studies which used laser scanning technology to monitor microtopographic changes (Table A5). This is because previous studies applied expensive laser scanning for the estimation of sediment redistribution, and due to the costs of the instrument it was not left in the field for continuous measurements, and hence research sites had to be revisited for each measurement (Nasermoaddeli und Pasche 2008; Eltner et al. 2016a; Eltner et al. 2016b; Hänsel et al. 2016). The estimated costs in studies using time-lapse photogrammetry were similar to our study (up to 5000 USD) (James und Robson 2014; Galland et al. 2016; Mallalieu et al. 2017; Eltner et al. 2017; Kromer et al. 2019; Blanch et al. 2021). However, time-lapse monitoring needs several devices set up in different viewing angles, which increases installation efforts and disturbance significantly.

In terms of data quality, our ToF device is more precise or comparable to those employed in earlier studies using ToF. The accuracy of the camera ($R^2 = 0.77$) was in the range of previous studies ($R^2 = 0.26$–0.83 (Eitel et al. 2011), Table A5). The horizontal point spacing of our cameras was 0.32 cm, and the maximum number of points per cm^2 was 8.5. These values are similar to previous studies in which the used devices had a horizontal point spacing in the range of 0.25–0.57 cm (Kaiser et al. 2014; Nasermoaddeli und Pasche 2008)) (Table A5), and the maximum number of points per cm^2 in a range of 1 point–25 points cm^{-2} (Eitel et al. 2011; Longoni et al. 2016) (Table A5).

Our cameras tended to slightly overestimate or underestimate the volume of redistributed sediment. This error occurs when the pulse reflects from several vertical objects such as walls or, in our case, branches or stones and then enters the camera sensor. This phenomenon was also observed in previous studies applying laser scanners and is inevitable if the goal is to study surface changes under natural field conditions

(Kukko und Hyyppä 2009; Ashcroft et al. 2014). During operation of the cameras, we learnt that our newly developed instruments are particularly capable of delivering usable scans at night. This is likely due to the strong scattered sunlight reaching the camera sensor during the day, blurring the data (Li 2014). Thus, in future studies, we recommend focusing on nocturnal operation to prevent light contamination.

5.2 The role of climate variability and burrowing cycles

We have found that rainfall plays a key role in triggering burrowing activity, which means that wet seasons experience higher sediment redistribution rates than dry seasons. In the year of investigation (2019), the dry season lasted from January until April, and from September until December (8 months), and the wet season lasted from May until August (4 months). The monitoring period lasted from March until October which covered 3 dry and 4 wet months (7 months in total). A yearly rate of sediment redistribution can be calculated by simply averaging the redistribution rate of the 7 monitored months and multiplying this result by 12 months, which results in an average redistribution rate of 0.4 m^2 ha^{-1} $year^{-1}$ for LC and 0.1 m^2 ha^{-1} $year^{-1}$ for PdA. However, because burrowing activity and rain-driven sediment redistribution is mainly determined by rainfall, this method might have led to an overestimation of the annual redistribution rate based on averaging, because the unmonitored part of the year 2019 was predominantly dry (Übernickel et al. 2021a). This can be accounted for by adding five times the dry month redistribution rate to the monitored 7 months, which leads to a lower annual redistribution rates for LC of 0.3 m^2 ha^{-1} $year^{-1}$ and for PdA of 0.1 m^2 ha^{-1} $year^{-1}$. Our values might thus overestimate sediment redistribution for the year 2019. This difference between both values (0.1 m^2 ha^{-1} $year^{-1}$ for LC and under 0.1 m^2 ha^{-1} $year^{-1}$ for PdA) can be interpreted as the uncertainty range for the year of observation.

However, decadal rainfall variability indicates that the year of monitoring (2019) was among the drier years of the last 30 years (Yáñez et al. 2001; Valdés-Pineda et al. 2016; Garreaud et al. 2002; Wilcox et al. 2016). The amount of precipitation since 1980 ranges from 200 mm until 800 mm per year (https://climatologia.meteochile.gob.cl/application/requerimiento/producto/RE3005) while the amount of precipitation in 2019 was just above 100 mm. This means, our results might underestimate sediment redistribution on a longer time perspective by 2 - 7 times.

Furthermore, the phenology of the burrowing animals is an additional source for uncertainty when calculating annual rates. The most common burrowing animal families in the area are active for three months of the year. The months in which they are active, are between April and September. None of the most common burrowing animal families were reported to be active from November until February. (Eccard und Herde 2013; Jimenez et al. 1992; Katzman et al. 2018; Malizia 1998; Monteverde und Piudo 2011). This is also in line with our observations, because burrowing intensity increased from March until May, reached its peak between May and June and declined until September (Figure 6). By extrapolating from 7 months to one-year period, our estimated excavation was 0.7 m^2 ha^{-1} $year^{-1}$ in LC and 0.8 m^2 ha^{-1} $year^{-1}$ in PdA. By adding five times the low active months to the 7 months of observation, the estimated excavation would be 0.6 m^2 ha^{-1} $year^{-1}$ in LC and 0.6 m^2 ha^{-1} $year^{-1}$ in PdA. Our values might thus overestimate the sediment excavation and the excavation uncertainty range is 0.1 m^2 ha^{-1} $year^{-1}$ for LC and 0.2 m^2 ha^{-1} $year^{-1}$ for PdA.
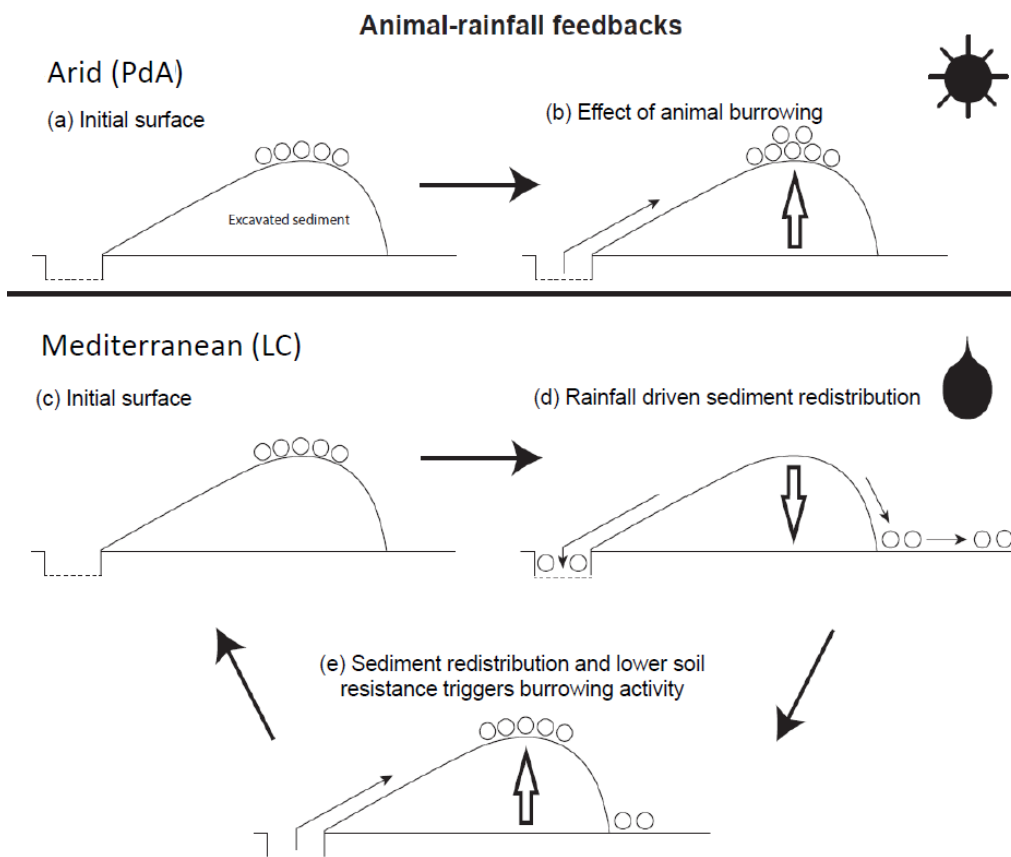
5.3. Sediment Redistribution

Our research reveals that the presence of vertebrate burrows generally increases hillslope sediment redistribution. We show, however, that the ratio between the sediment redistribution caused by rainfall within

634 burrow and burrow embedding areas varies between climate zones. Sediment redistribution within burrow
635 areas was 40% higher at the arid research site, and at the mediterranean research site, it was 338% higher
636 when compared to burrow embedding area (Table A6).
637   By monitoring microtopographical changes in a high spatio-temporal resolution, we found that the
638 occurrence of larger rainfall events played a two-fold, accelerating role in influencing sediment redistribution
639 (Fig. 9). Firstly, rainfall-runoff eroded burrow material caused increased sediment loss. This was followed by
640 animal burrowing activity after the rainfall. This means that rainfall triggered animal burrowing activity which
641 was very likely related to a lower burrowing resistance of the soil due to the increased soil moisture (Rutin
642 1996; Romañach et al. 2005; Herbst und Bennett 2006). This double feedback led to frequently occurring but
643 small redistribution rates. However, cumulatively, the mechanism increased downhill sediment fluxes. Previous
644 studies most likely missed this low magnitude but frequent surface processes due to a lower monitoring
645 duration and frequency, or artificial laboratory conditions, and thus, did not quantify the full volume of
646 redistributed sediment associated with burrowing activity. To quantify all occurred sediment redistribution
647 processes, a continuous surface monitoring, like the here presented, is needed.
648

Figure 9. Scheme of animal-driven and rainfall-driven sediment redistribution processes in both investigated climate zones: (**a**) Describes the initial surface of the burrow before the start of a sediment redistribution process, and (**b**) the animal excavation process in the arid climate zone. Here, due to rarely occurring rainfall events, sediment redistribution is mostly controlled by the animal burrowing activity; (**c**) describes the initial burrow surface in the mediterranean climate zone, (**d**) the process of sediment redistribution during a rainfall event and (**e**) the subsequent animal burrowing activity. Burrowing is triggered by decreased soil resistance due to the increased soil moisture after rainfall as well as by sediment accumulation within the burrow's entrance. Burrowing activity leads to a new supply of sediment being excavated to the surface. In the

23

658 mediterranean climate zone, sediment redistribution is controlled by both animal burrowing activity and rainfall.
659 The alternating excavation and erosion process ultimately lead to an increase in redistribution rates.
660

661 Our results indicate an up to 338% increase in the sediment volume redistributed during rainfall events
662 measured within burrows when compared to burrow embedding areas. In contrast to our result, the maximum
663 increase estimated in previous studies was 208% (Table A6, (Imeson und Kwaad 1976). The two climate
664 zones also show different patterns: In the mediterranean climate, the contribution of animals' (vertebrates')
665 burrowing activity appear larger than previously observed by using field methods such as erosion pins or
666 splash traps (from –3% until – 208%, Table A6, (Imeson und Kwaad 1976; Hazelhoff et al. 1981; Black und
667 Montgomery 1991). In contrast, in arid PdA, our study found a much smaller increase (40%, Table A6) in the
668 sediment volume redistributed during rainfall events measured within burrows when compared to burrow
669 embedding areas. This is lower than previously estimated (125%, Table A6, (Black und Montgomery 1991).
670 However, solely one rainfall event above 0.2 mm day^{-1} occurred during our monitoring period. Hence, we
671 conclude that the contribution of burrowing activity of animals to hillslope sediment transport is much larger in
672 areas with frequent rainfall events than previously thought, while it has been realistically estimated by previous
673 studies for areas with rare rainfall events (Table A6).

674   Magnitudes of sediment volume redistributed within burrows similar to our results were previously
675 obtained solely in studies applying rainfall simulators. These studies estimated an increase in the volume of
676 sediment redistributed during rainfall events, measured within burrows when compared to burrow embedding
677 areas, to be between 205% and 473% (Table A6, (Li et al. 2018; Chen et al. 2021). However, a rainfall simulator
678 can only provide data on surface processes within a plot of a few m^2 in size and under ideal laboratory
679 conditions while ignoring the uphill microtopography, vegetation cover and distribution (Iserloh et al. 2013),
680 which were shown to reduce erosion rates. More importantly, the rainfall intensity on hillslopes decreases with
681 (i) the angle of incidence of the rain, (ii) the inclination of the surface and iii) the relative orientation of the
682 sloping surface to the rain vector (Sharon 1980). When simulating a rainfall event with the same rainfall volume
683 as in the field, the rain is induced directly over the treated surface and has thus a higher velocity which leads
684 to an increased splash erosion than under natural conditions (Iserloh et al. 2013). We thus propose that the
685 rainfall experiments overestimate the erosion rate while the correct erosion rate can be measured solely under
686 field conditions.

687   Cumulative sediment redistribution within burrow roof, mound and entrance was, on average, 28%
688 lower than cumulative sediment redistribution only within the mound and the burrow roof (Figure A7). These
689 results suggest that 28% of the eroded sediment from animal mounds and burrow roofs is re-accumulated
690 within the burrow entrance during rainfall-runoff events, and the remaining 62% is incorporated into overall
691 hillslope sediment flux. Our numbers contrast with previous studies, which quantified that about 58% of the
692 sediment excavated by animals will accumulate back in the burrow entrance and only 42% is incorporated to
693 downhill sediment flux (Andersen 1987; Reichman und Seabloom 2002). Hence, our results indicate not only
694 higher redistribution rates within burrows by burrowing animals but also point to much higher supply of
695 sediment to the downhill sediment flux than previously thought.

696   Our cost-effective ToF device provides data on surface changes in a high spatio-temporal resolution.
697 The high temporal resolution was able to unravel ongoing low magnitude but frequent animal excavation and
698 erosion processes. The high spatial resolution enabled us to estimate the exact volume of sediment fluxes
699 from the burrows downhill. The here presented results indicate that the contribution of burrowing animals on

the burrow as well as on the hillslope scale was much higher than previously assumed. Our results can be integrated into long-term soil erosion models that rely on soil processes and improve their accuracy by including animal-induced surface processes on microtopographical scales in their algorithms.

Institutional Review Board Statement: Not applicable.

Informed Consent Statement: Not applicable.

Competing interests: There is no conflict of interest.

Author contribution: JB, AL and SA planned the campaign; PG and SA performed the measurements; PG analysed the data and wrote the manuscript draft; AL, JB, NF, RB, KÜ, LP, CR, DK and PP reviewed and edited the manuscript.

Code/Data availability: Code and all raw data can be provided by the corresponding author upon request.

Appendices

Table A1. List of abbreviations

α [°]	Tilt angle of the camera
b [°]	Surface inclination
Ω	Threshold value for the scan scattering error
B	Burrow
Area$_{burrow}$	mean in the field measured size of the burrows which are monitored
Area	total surface area monitored by the camera
BD	Bulk density
c [m/s]	Speed of light
D	Distance from the camera to the object
Dens$_{burrow}$	Burrow density
DSM	Digital surface model
DSM$_{after}$	DSM calculated from the scan taken after the extraction
DSM$_{before}$	DSM calculated from the scan taken before the extraction
EM	Burrow embedding area
Entrance	entrance to the animal burrow
g [-]	ratio [-] of the reflected photons to all photons
LC	National Park LC
LC-NL	Camera in LC on the lower north-facing hillslope
LC-NU	Camera in LC on the upper north-facing hillslope
LC-SL	Camera in LC on the lower south-facing hillslope
LC-SU	Camera in LC on the upper south-facing hillslope

MAE	Mean absolute error
MAP [°]	Mean annual precipitation
m.a.s.l.	Meters above sea level
MAT	Mean annual temperature
mClay [%]	Mean content of clay
mean$_{z\text{-coordinate}}$	Mean value of the z-coordinates
Mound	the sediment excavated by the animal while digging the burrow
mSand [%]	Mean content of sand
mSilt [%]	Mean content of silt
n	Number of scans
PdA	National Park Pan de Azúcar
PdA-NL	Camera in PdA on the lower north-facing hillslope
PdA-NU	Camera in PdA on the upper north-facing hillslope
PdA-SL	Camera in PdA on the lower south-facing hillslope
PdA-SU	Camera in PdA on the upper south-facing hillslope
Res	Resolution
Roof	sediment pushed aside and uphill the entrance during burrow creation
S$_a$	scan after the rainfall event
S$_b$	scan before the rainfall event
SBC	Single board computer
sd$_{z\text{-coordinate}}$	standard deviation of the z-coordinates
SSH	Secure shell
t [s]	Overall time of camera illumination
TOC [%]	Total organic carbon
ToF	Time-of-Flight
Vol$_{burrow}$	volume of redistributed sediment within burrow
Vol$_{detected}$	volume of the extracted sediment as detected by the camera
Vol$_{add}$	difference in redistributed sediment volume between burrows and burrow embedding areas
Vol$_{exc}$	Volume of the sediment excavated by the animal
Vol$_{hillslope\text{-wide}}$	Hillslope-wide volume of redistributed sediment
Vol$_{measured}$	volume of the extracted sediment measured by the measuring cup
Vol$_{per\ burrow}$	Volume of redistributed sediment per burrow
Vol$_{per\ pixel}$	Volume of redistributed sediment per pixel
Vol$_{redistributed}$	volume of the calculated redistributed sediment
Vol$_{embedding}$	volume of redistributed sediment within burrow embedding area
y$_i$	distance of the point to the point of origin at the camera nadir
z$_{cor}$	Corrected z-coordinate
z$_{uncor}$	Uncorrected z-coordinate

720

721 **Table A2.** Number of usable scans for each camera

Camera	Latitude	Longitude	Number of scans	Percentage of usable scans taken at 1am / 5am / 8am / 10pm	Time period
PdA-NU	-25.98131	-70.6166	238	29 / 27 / 20 / 24	18.3.-18.9.
PdA-NL	-25.98277	-70.61278	52	24 / 0 / 40 / 36	27.3.-31.5
PdA-SU	-25.97477	-70.61641	351	30 / 26 / 32 / 11	16.3.-19.9.
PdA-SL	-25.97177	-70.61409	167	48 / 38 / 7 / 8	16.3.-19.9.
LC-NU	-32.95230	-71.06231	215	37 / 20 / 8 / 33	9.3.-9.9.
LC-NL	-32.93928	-71.08613	3	-	6.3.-12.9
LC-SU	-32.93078	-71.09066	160	22 / 28 / 26 / 25	28.3.-22.5
LC-SL	-32.93110	-71.08987	167	27 / 25 / 22 / 26	16.3.-19.9.

722

723 **Table A3.** Summary of the volume of redistributed sediment, according to area and disturbance type. Vol_{exc}
724 describes volume of the sediment excavated by the animals. Vol_{burrow} describes volume of the sediment
725 redistributed during rainfall events within burrows. Vol_{add} describes the difference in redistributed sediment
726 volume within burrows and burrow embedding area during rainfall.

Disturbance	Area	PdA	LC
Vol_{exc}	Burrow	16.41 cm^3 cm^{-2} $year^{-1}$	14.62 cm^3 cm^{-2} $year^{-1}$
	Per burrow	1498.66 cm^3 $burrow^{-1}$ $year^{-1}$	1226.61 cm^3 $burrow^{-1}$ $year^{-1}$
	Hillslope-wide	0.18 m^3 ha^{-1} $year^{-1}$	0.67 m^3 ha^{-1} $year^{-1}$
Vol_{burrow}	Burrow	-1.97 cm^3 cm^{-2} $year^{-1}$	-10.44 cm^3 cm^{-2} $year^{-1}$
	Per burrow	-126.36 cm^3 $burrow^{-1}$ $year^{-1}$	-876.38 cm^3 $burrow^{-1}$ $year^{-1}$
	Hillslope-wide	-0.05 m^3 ha^{-1} $year^{-1}$	-0.48 m^3 ha^{-1} $year^{-1}$
Vol_{add}	Burrow	-1.18 cm^3 cm^{-2} $year^{-1}$	-7.37 cm^3 cm^{-2} $year^{-1}$
	Per burrow	-48.36 cm^3 $burrow^{-1}$ $year^{-1}$	-619.2 cm^3 $burrow^{-1}$ $year^{-1}$
	Hillslope-wide	-0.02 m^3 ha^{-1} $year^{-1}$	-0.34 m^3 ha^{-1} $year^{-1}$

727
728

729 **Table A4.** Summary of the volume of redistributed sediment, according to area and disturbance type. Vol_{exc}
730 describes volume of the sediment excavated by the animals. Vol_{burrow} describes volume of the sediment
731 redistributed during rainfall events within burrows. Vol_{add} describes the difference in redistributed sediment
732 volume within burrows and burrow embedding areas during rainfall.

Disturbance	Area	PdA	LC
Vol_{exc}	Burrow	9.57 cm^3 cm^{-2} 7 $months^{-1}$	8.53 cm^3 cm^{-2} 7 $months^{-1}$
	Per burrow	874.22 cm^3 $burrow^{-1}$ 7 $months^{-1}$	715.52 cm^3 $burrow^{-1}$ 7 $months^{-1}$
	Hillslope-wide	0.11 m^3 ha^{-1} 7 $months^{-1}$	0.39 m^3 ha^{-1} 7 $months^{-1}$
Vol_{burrow}	Burrow	-1.15 cm^3 cm^{-2} 7 $months^{-1}$	-6.09 cm^3 cm^{-2} 7 $months^{-1}$
	Per burrow	-73.71 cm^3 $burrow^{-1}$ 7 $months^{-1}$	-511.22 cm^3 $burrow^{-1}$ 7 $months^{-1}$

	Hillslope-wide	-0.03 m^3 ha^{-1} 7 months^{-1}	-0.28 m^3 ha^{-1} 7 months^{-1}
Vol$_{add}$	Burrow	-0.69 cm^3 cm^{-2} 7 months^{-1}	-4.30 cm^3 cm^{-2} 7 months^{-1}
	Per burrow	-28.21 cm^3 burrow^{-1} 7 months^{-1}	-361.20 cm^3 burrow^{-1} 7 months^{-1}
	Hillslope-wide	-0.01 m^3 ha^{-1} 7 months^{-1}	-0.2 m^3 ha^{-1} 7 months^{-1}

733

734 **Table A5.** Review of studies which used laser scanners for the estimation of surface processes.

Reference	R^2	Error	Horizontal point spacing	Points per cm^{-2}	Model	Price
Our results	0.77	0.15 cm	0.32 cm	8.5	Texas Instruments OPT3101	900 USD
(Eitel et al. 2011)	0.23-0.86	0.07 cm	NA	25	Leica ScanStation 2	102 375 USD
(Eltner et al. 2013)	NA	0.4 cm	NA	6.4	Riegl LMS-Z420i	16 795 USD
(Kaiser et al. 2014)	NA	NA	0.57 cm	NA	Riegl LMS-Z420i	16 795 USD
(Longoni et al. 2016)	NA	NA	NA	1	Riegl LMS-Z420i	16 795 USD
(Morris et al. 2011)	NA	0.5 cm	NA	NA	Maptek I-Site 4400LR	240 000 USD
(Nasermoaddeli und Pasche 2008)	NA	0.2 cm	0.25 cm	NA	Leica Cyrax HDS 2500	4500 USD
(Thomsen et al. 2015)	NA	NA	0.4 cm	NA	Leica ScanStation 2	102 375 USD

735

736 **Table A6.** Review of studies which estimated the sediment redistribution within burrows and burrow embedding
737 areas and the proposed impact.

Reference	Climate	Animals	Method	Monitoring period	Frequency	Burrows	Burrow embedding area	impact
(Imeson und Kwaad 1976)	continental	Rodents	erosion pins	15 months	monthly	20 mm		NA
(Imeson und Kwaad 1976)	continental	Rodents	splash boards	15 months	monthly	91.75g 24.49 cm^{-2} = 3.75 cm^3 cm^{-2}	94g	-3%

Study	Climate	Animal	Method	Duration	Frequency	With burrow	Without burrow	%
(Imeson und Kwaad 1976)	continental	Rodents	rainfall simulation (7.5 cm / hour intensity)	One-time measurement	NA	0.2 g – 0.73 g	0.009 g – 0.23 g	+208%
(Imeson 1977)	continental	Vertebrates	rainfall simulation	One-time measurement	NA	0.18-0.3 100 J^{-1} m^{-2} rain	0.146 100 J^{-1} m^{-2} rain	+123%
(Hazelhoff et al. 1981)	continental	Earthworms	splash traps	12 months	monthly	NA	NA	+180%
(Black und Montgomery 1991)	arid	pocket gopher	erosion pins	10 months	2 months	NA	NA	+125%
(Hakonson 1999)	temperate	pocket gophers	rainfall simulator (60 mm / hour)	2 years	2 – 3 weeks	2.4 – 8.7 mg ha^{-1}	4.4 – 15 mg ha^{-1}	-43%
(Li et al. 2018)	temperate	mole crickets	rainfall simulation (36 mm / hour)	One time measurement	15 measurements	22.1 g 115 cm^{-2} = 5.2 cm^3 cm^{-2}	5 g 123 cm^{-2} = 1.09 cm^3 cm^{-2}	+473%
(Li et al. 2018)	temperate	mole crickets	rainfall simulation (36 mm / hour)	One time measurement	15 measurements	35.3 g 220.5 cm^{-2} = 6.24 cm^3 cm^{-2}	5 g 123 cm^{-2} = 1.09 cm^3 cm^{-2}	+473%
(Chen et al. 2021)	lab	chinese zocor	rainfall simulation (80 mm / hour)	One-time measurement	3 measurements	2,69 g cm^{-2} = 2.69 cm^3 cm^{-2}	0,88 g cm^{-2} = 0.88 cm^3 cm^{-2}	+205%

738

739

740 **Table A7.** Review of studies which estimated the sediment redistribution within burrows, average burrow
741 density as found in the literature and area-wide yearly contribution of burrowing animals to sediment
742 redistribution.

Climate	Animals	Burrows	Average burrow density	Average burrow size	Area-wide redistribution
Continental	Rodents	91.75g 24.49 cm^{-2} = 3.75 cm^3 cm^{-2} (Imeson und Kwaad 1976)	14 625 m^{-2} = 0.02 m^{-2} (Pang und Guo 2017)	24.49 cm^2 (Imeson und Kwaad 1976)	0.183 m^3 ha^{-1} year^{-1}
Temperate	mole crickets	22.1 g 115 cm^{-2} = 5.2 cm^3 cm^{-2} (Li et al. 2018)	405 ha^{-1} (Castner und Fowler 1984)	115 cm^2 (Li et al. 2018)	0.24 m^3 ha^{-1} year^{-1}
Temperate	mole crickets	35.3 g 220.5 cm^{-2} = 6.24 cm^3 cm^{-2} (Li et al. 2018)	405 ha^{-1} (Castner und Fowler 1984)	220.5 cm^2 (Li et al. 2018)	0.56 m^3 ha^{-1} year^{-1}
Lab	chinese zocor	2,69 g cm^{-2} = 2.69 cm^3 cm^{-2} (Chen et al. 2021)	94.69 2500m^{-2} = 0.04 m^{-2} = 400 ha^{-1}	1256 cm^2	1.35 m^3 ha^{-1} year^{-1}

743

744 **Table A8.** Review of studies which estimated the volume of sediment excavated by burrowing animals.

	Climate	Animals	Method	Monitoring period	Frequency	volume of the excavated sediment
(Black und Montgomery 1991)	Arid	porcupines	mound volume	3 years	yearly	0.2 m^3 ha^{-1} year^{-1}
(Black und Montgomery 1991)	Arid	isopods	mound volume	3 years	yearly	0.11 m^3 ha^{-1} year^{-1}
(Black und Montgomery 1991)	Arid	pocket gopher	mound volume	2 years	3 model runs	0.05 – 0.11 m^3 ha^{-1} year^{-1}
(Rutin 1996)	Subtropical	scorpions	mound volume	6 months	2-29 days	0.42 m^3 ha^{-1} year^{-1}
(Hall et al. 1999)	Alpine	rodents	mound volume	1 year	yearly	0.02 m^3 ha^{-1} year^{-1}
(Hall et al. 1999)	Alpine	bears	mound volume	1 year	yearly	0.49 m^3 ha^{-1} year^{-1}
(Yoo et al. 2005)	Arid	pocket gopher	mound volume	1 year	One model run	0.1-0.2 m^3 ha^{-1} year^{-1}

745
746
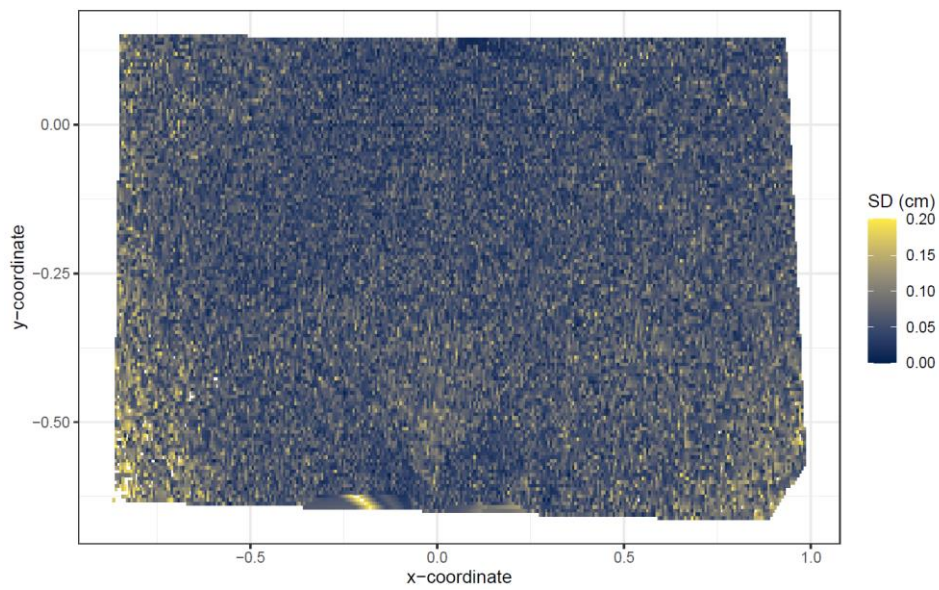
747
748 **Figure A1.** Standard deviation of the z-coordinate of unprocessed five scans showed exemplary for the camera
749 on the upper north-facing hillside. SD is standard deviation. The error increases with distance from the camera
750 nadir point. The standard deviation was here calculated from scans before any corrections.
751
752
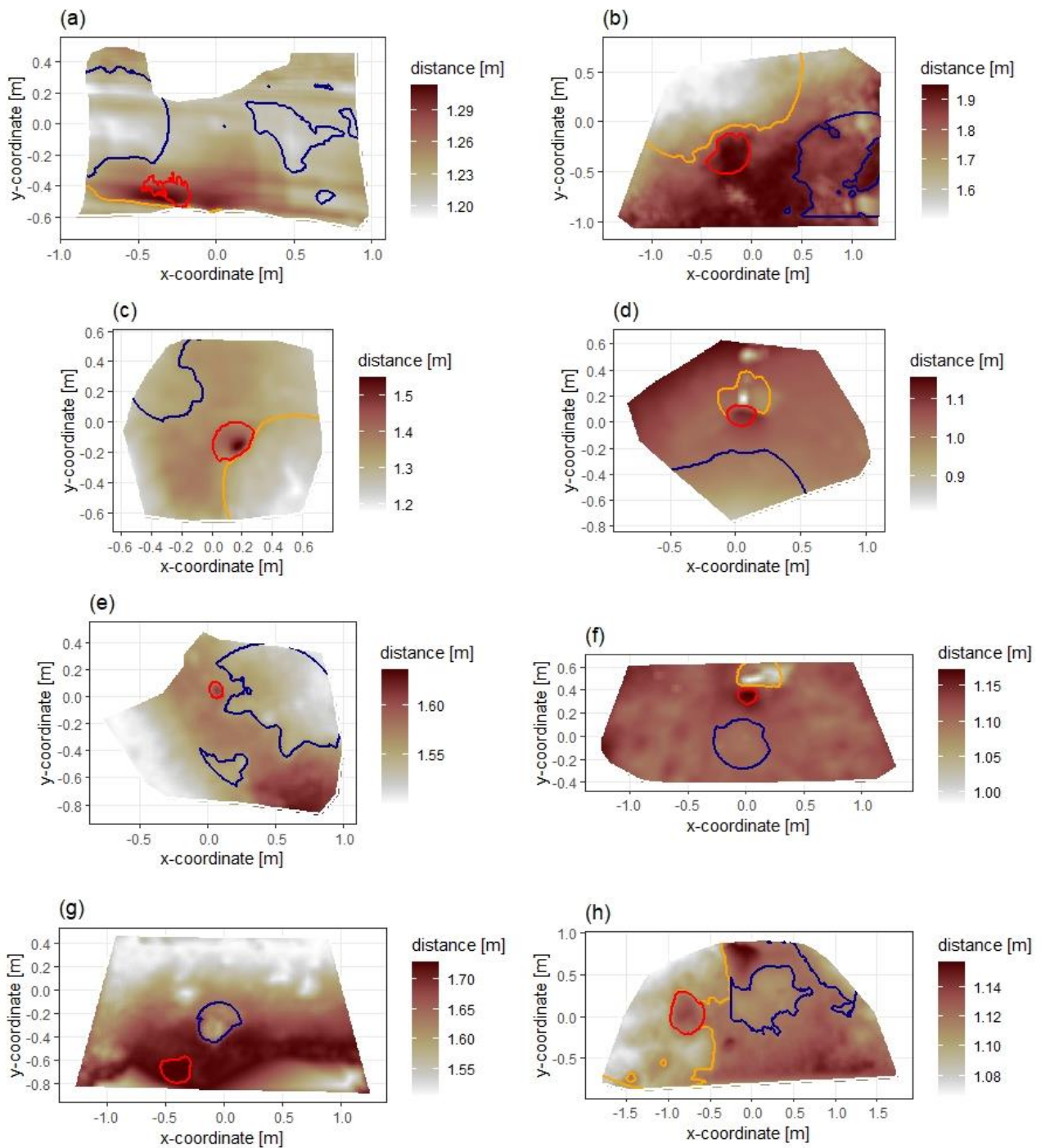
Figure A2. Delineation of the areas. The point of origin of the coordinate system is at the camera nadir. Depth is the distance between the surface and the camera. Red is the outline of the burrow entrance. Green is the outline of mound. Orange is the outline of burrow roof. Area which is not outlined is burrow embedding area. Arrow indicates downhill direction of the hillslope. (a) LC-NU. (b) LC-NL (c) LC-SU. (d) LC-SL. (e) PdA-NU. (f) PdA-NL. (g) PdA-SU. (h) PdA-SL.
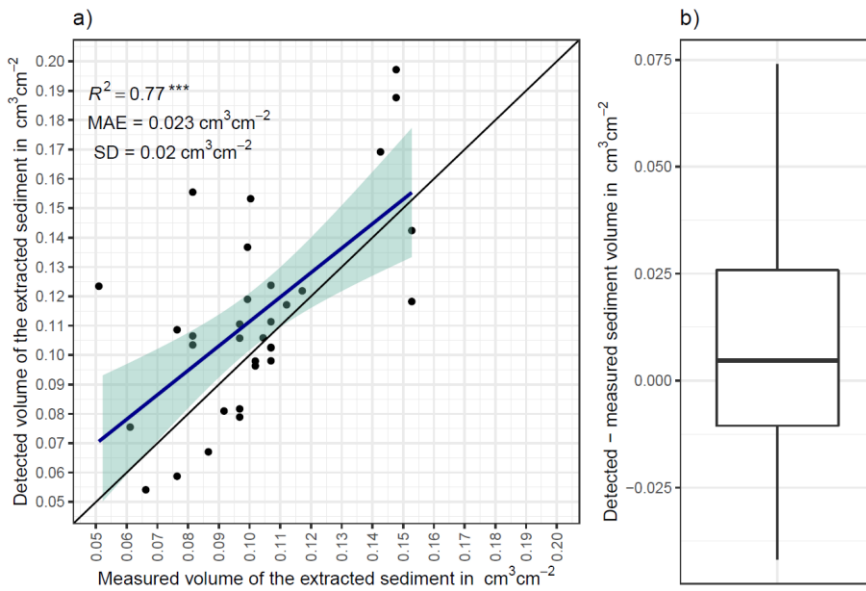
759

760 **Figure A3.** a) Estimation of Time-of-Flight camera accuracy based on averaging two surface scans before and
761 after the sediment extraction under controlled conditions. The *x*-axis shows the exact sediment volume
762 measured with a cup. The *y*-axis represents the volume of the sediment calculated from the camera scans
763 (according to Equation (4)). The blue line is the linear regression calculated from the measured and detected
764 volume. The green shadow shows the confidence interval of 95% for the linear regression slope. ***$p \leq 0.001$.
765 MAE is the mean absolute error, SD is standard deviation and R^2 the coefficient of determination. b) Measured
766 sediment volume subtracted from the detected sediment volume for all measurements.

767
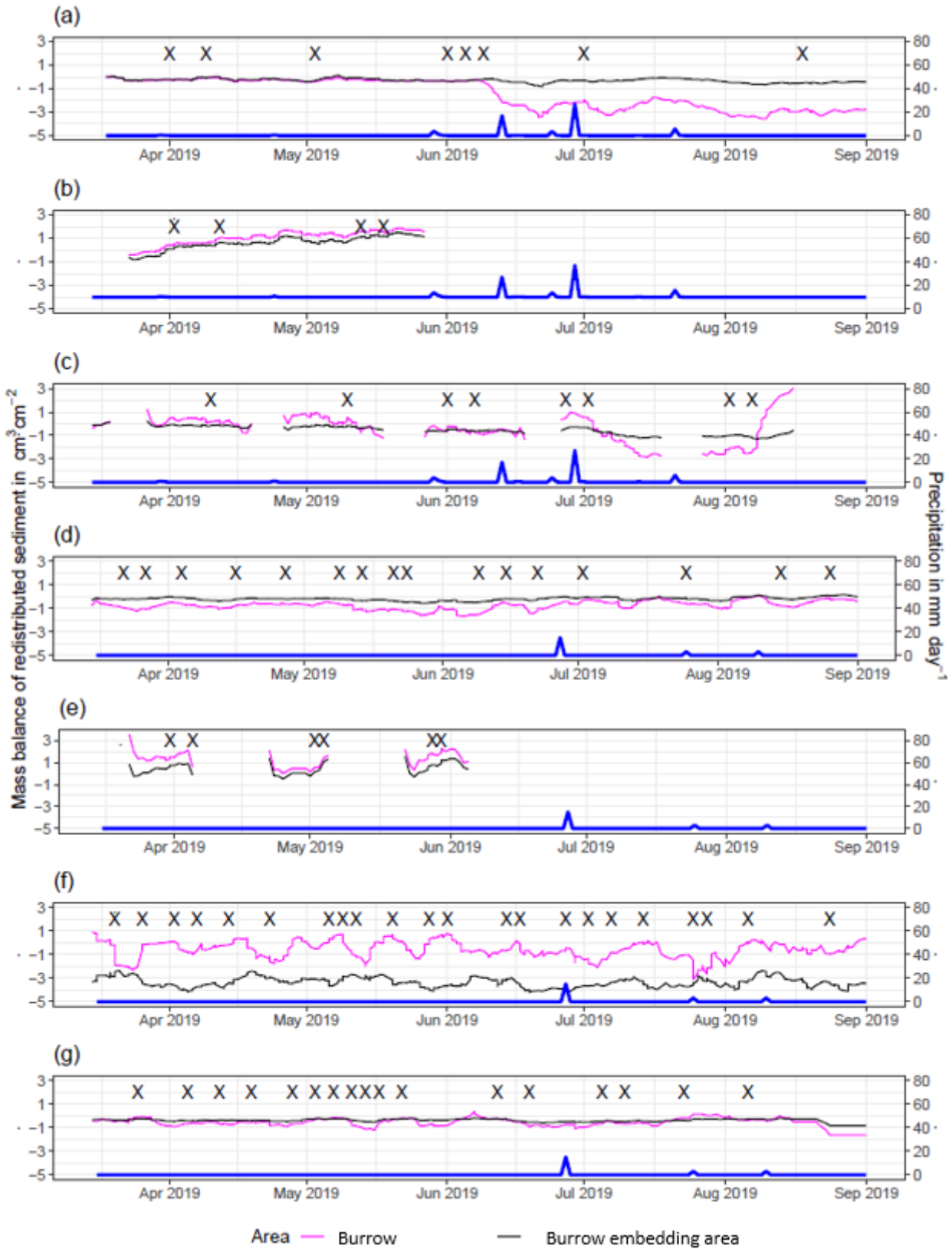
Figure A4. Sediment mass balance for the period of 7 months separately for burrows and burrow embedding areas as measured by the cameras. (a) LC-NU. (b) LC-SU. (c) LC-SL. (d) PdA-NU. (e) PdA-NL. (f) PdA-SU. (g) PdA-SL. For abbreviations see Table A1.
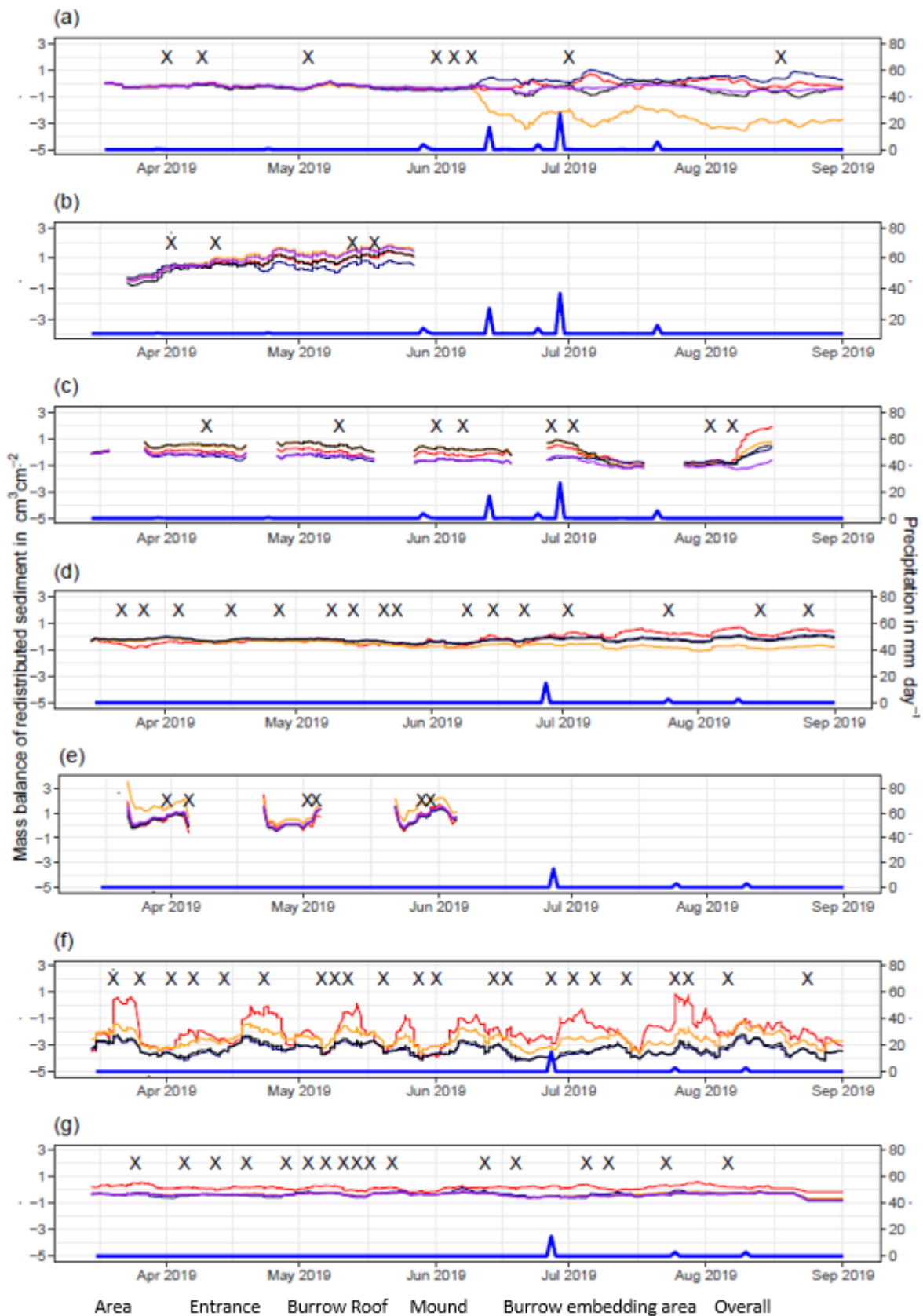
Figure A5. Sediment mass balance for the period of 7 months separately for all delineated areas as measured by the cameras. (a) LC-NU. (b) LC-SU. (c) LC-SL. (d) PdA-NU. (e) PdA-NL. (f) PdA-SU. (g) PdA-SL. For abbreviations see Table A1.
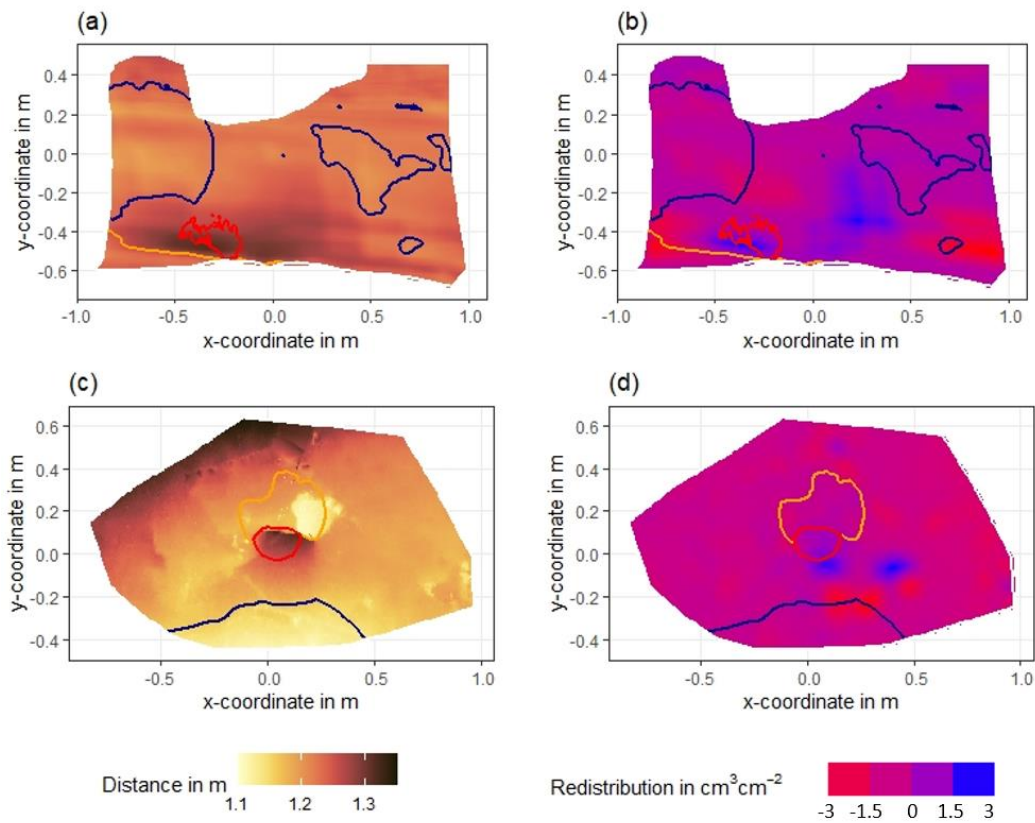
Figure A6. Examples of surface scans showing the digital surface model (DSM) before a rainfall event (**a**, **c**) at two camera locations in La Campana, and the calculated volume of redistributed sediment (**b**, **d**) after the rainfall event: (**a**) DSM of a scan from the camera on the upper north-facing hillslope in La Campana; (**b**) Detected sediment redistribution (cm^3 cm^{-2}) on the upper north-facing hillslope in La Campana after a rainfall event of 17.2 mm day^{-1}; (**c**) DSM of a scan from the camera on the upper south-facing hillslope in La Campana; (**d**) Detected sediment redistribution (cm^3 cm^{-2}) on the upper south-facing hillslope after a rainfall event of 17.2 mm day^{-1}. Red is the outline of the burrow entrance. Green is the outline of mound. Orange is the outline of the burrow roof. The area which is not outlined is burrow embedding area. Redistribution is the volume of the redistributed sediment, either accumulated (positive value) or eroded (negative value) per cm^3 cm^{-2}. After the rainfall events, sediment mostly accumulated within the burrow entrance or near mounds and eroded from burrow roofs and mounds.
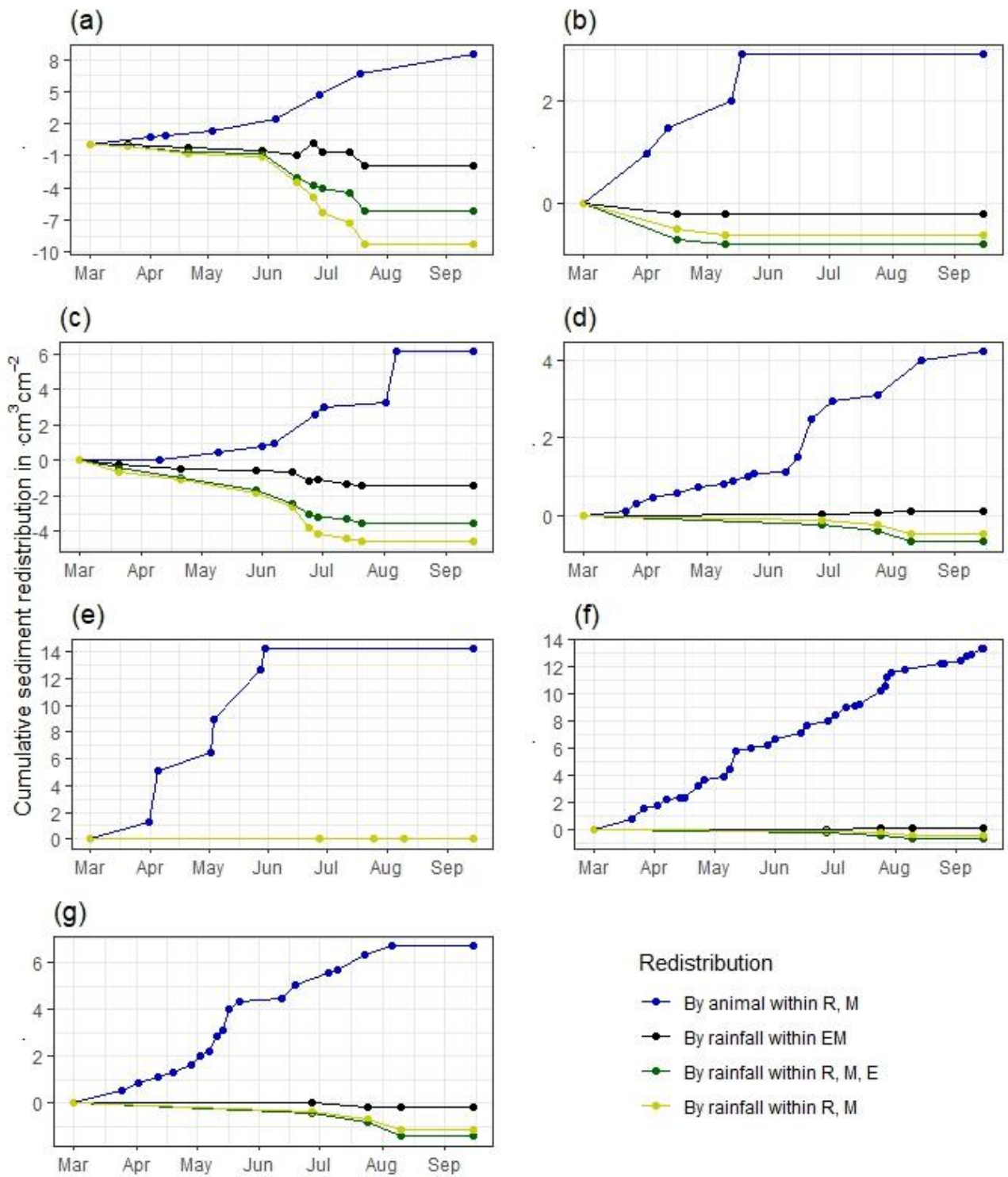
Figure A7. Cumulative volume of redistributed sediment for all cameras. Positive values indicate sediment accumulation. Negative values indicate sediment erosion. Whiskers are the median sediment redistribution. E is the burrow entrance. M is the mound. R is burrow roof. EM is burrow embedding area. LC is mediterranean climate zone. PdA is arid climate zone. (a) LC-NU. (b) LC-SU. (c) LC-SL. (d) PdA-NU. (e) PdA-NL. (f) PdA-SU. (g) PdA-SL. For abbreviations see Table A1.
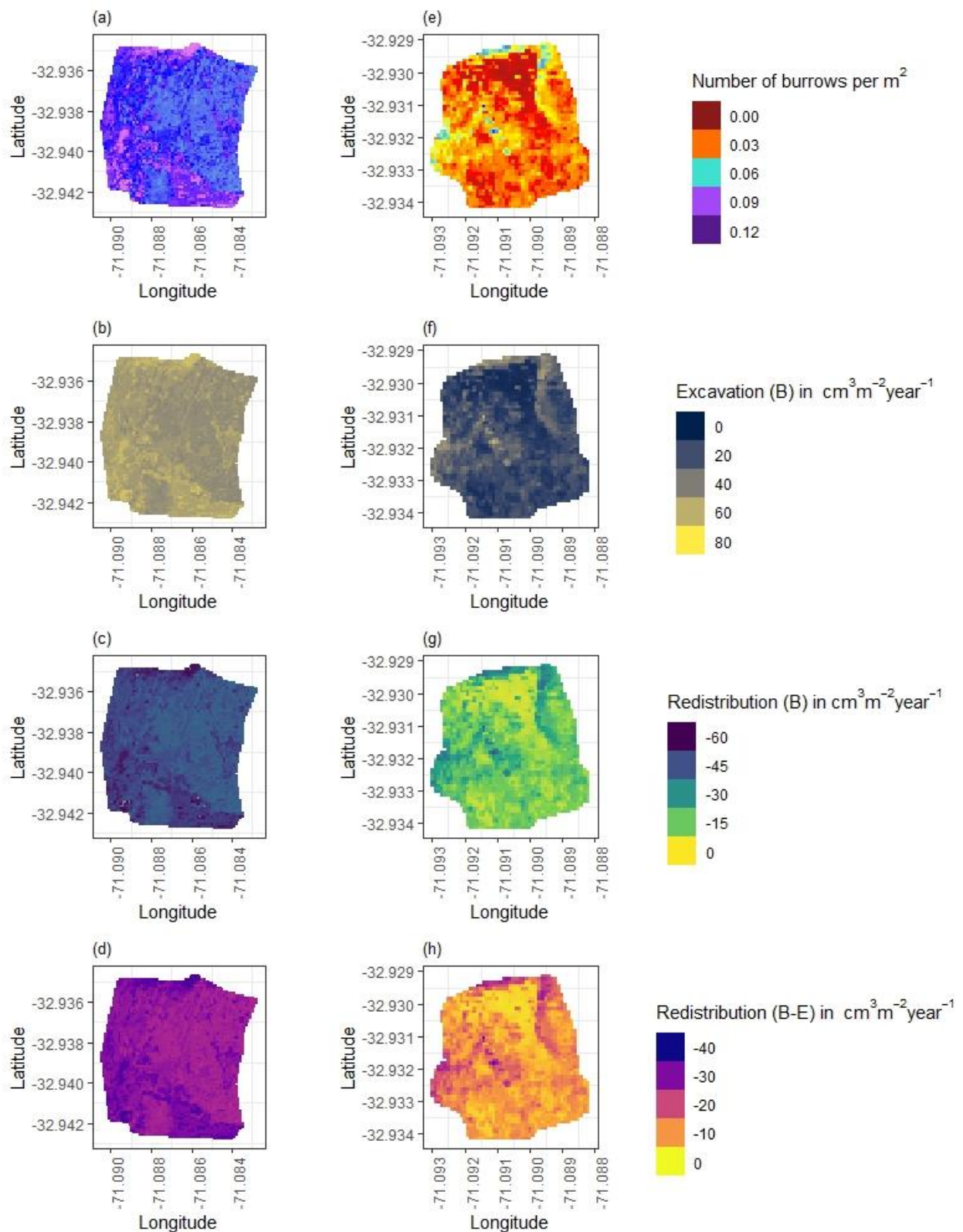
**Figure A8.** Hillslope-wide volume of redistributed sediment for a time period of one year in LC. (a-d) North-facing hillslope. (e-h) South-facing hillslope. (a) and (e) Density of burrows as estimated by Grigusova et al. 2021. (b) and (f) Volume of the sediment excavated by the animals. (c) and (g) Volume of the sediment redistributed during rainfall events within burrows. (d) and (h) Volume of additionally redistributed sediment during rainfall events due to presence of the burrows. The values were calculated per burrow as stated in section 3.7 by subtracting the sediment volume redistributed within burrows from the sediment volume

redistributed within burrow embedding area and then upscaled. B stays for burrow, EM stays for burrow
806 embedding area.
807
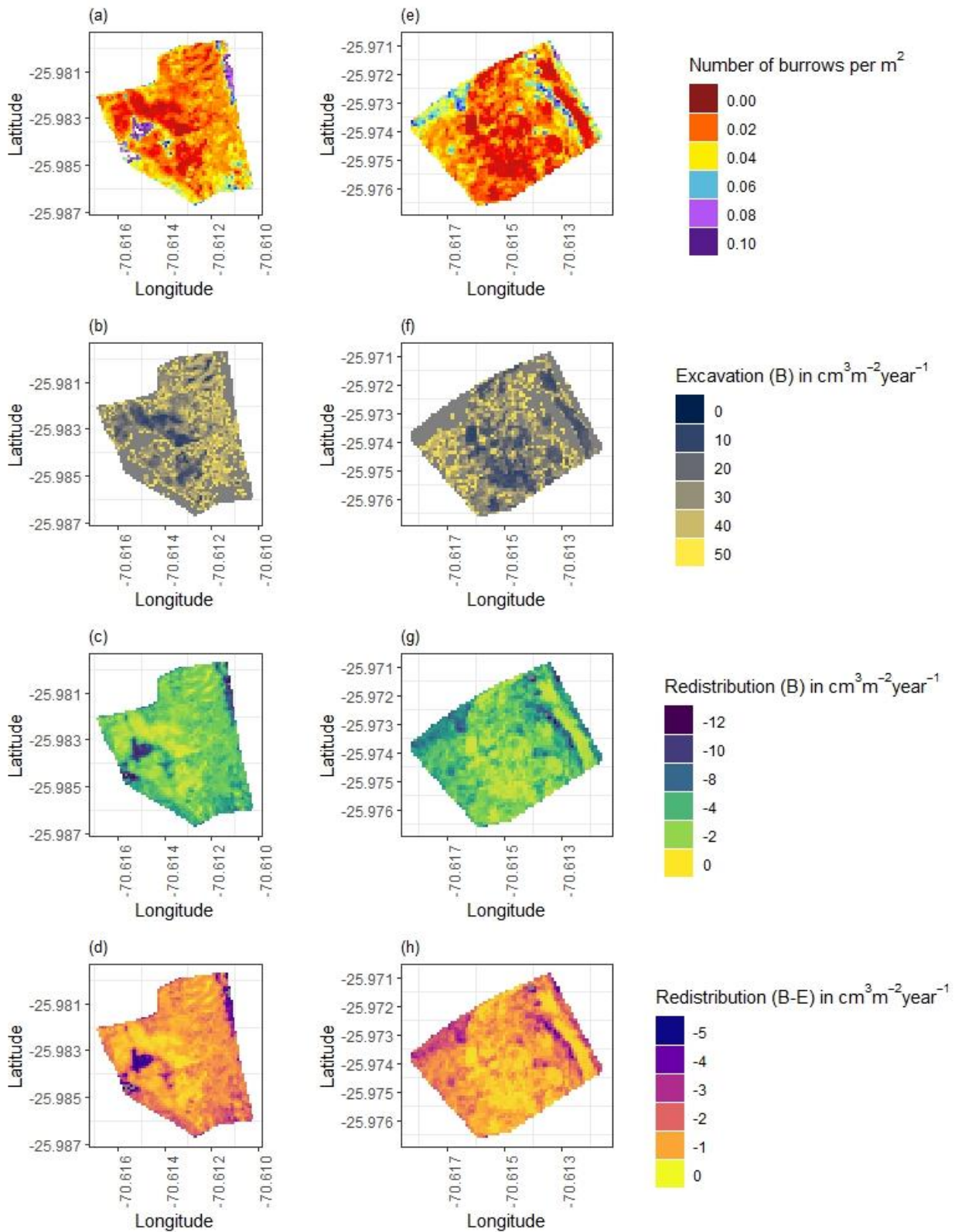
808
809 **Figure A9.** Hillslope-wide volume of redistributed sediment for a time period of one year in Pan de Azúcar. (a-
810 d) North-facing hillslope. (e-h) South-facing hillslope. (a) and (e) Density of burrows as estimated by Grigusova
811 et al. 2021. (b) and (f) Volume of the sediment excavated by the animals. (c) and (g) Volume of the sediment
812 redistributed during rainfall events within burrows. (d) and (h) Volume of additionally redistributed sediment

813 during rainfall events due to presence of the burrows. The values were calculated per burrow as stated in
814 section 3.7 by subtracting the sediment volume redistributed within burrow from the sediment volume
815 redistributed within burrow embedding area and then upscaled. B stays for burrow, EM stays for burrow
816 embedding area by the burrowing animal.
817

References

819 Afana, A.; Solé-Benet, A.; Pérez, J. L. (2010): Determination of Soil Erosion Using Laser Scanners.
820   Experimental Station of Arid Zone, CSIC, Almeria, Spain, zuletzt geprüft am 22.12.2021.
821 Andersen, Douglas C. (1987): Geomys Bursarius Burrowing Patterns: Influence of Season and
822   Food Patch Structure. In: *Ecology* 68 (5), S. 1306–1318. DOI: 10.2307/1939215.
823 Ashcroft, Michael B.; Gollan, John R.; Ramp, Daniel (2014): Creating vegetation density profiles
824   for a diverse range of ecological habitats using terrestrial laser scanning. In: *Methods Ecol Evol*
825   5 (3), S. 263–272. DOI: 10.1111/2041-210X.12157.
826 BANCROFT, W. J.; HILL, D.; ROBERTS, J. D. (2004): A new method for calculating volume of
827   excavated burrows: the geomorphic impact of Wedge-Tailed Shearwater burrows on Rottnest
828   Island. In: *Funct Ecology* 18 (5), S. 752–759. DOI: 10.1111/j.0269-8463.2004.00898.x.
829 Bernhard, Nadine; Moskwa, Lisa-Marie; Schmidt, Karsten; Oeser, Ralf A.; Aburto, Felipe; Bader,
830   Maaike Y. et al. (2018): Pedogenic and microbial interrelations to regional climate and local
831   topography: New insights from a climate gradient (arid to humid) along the Coastal Cordillera
832   of Chile. In: *CATENA* 170 (4), S. 335–355. DOI: 10.1016/j.catena.2018.06.018.
833 Black, Thomas A.; Montgomery, David R. (1991): Sediment transport by burrowing mammals,
834   Marin County, California. In: *Earth Surf. Process. Landforms* 16 (2), S. 163–172. DOI:
835   10.1002/esp.3290160207.
836 Blanch, Xabier; Eltner, Anette; Guinau, Marta; Abellan, Antonio (2021): Multi-Epoch and Multi-
837   Imagery (MEMI) Photogrammetric Workflow for Enhanced Change Detection Using Time-
838   Lapse Cameras. In: *Remote Sensing* 13 (8), S. 1460. DOI: 10.3390/rs13081460.
839 Castner, James L.; Fowler, H. G. (1984): Distribution of Mole Crickets (Orthoptera: Gryllotalpidae:
840   Scapteriscus) and the Mole Cricket Parasitoid Larra bicolor (Hymenoptera: Sphecidae) in Puerto
841   Rico. In: *The Florida Entomologist* 67 (3), S. 481. DOI: 10.2307/3494730.
842 Chen, Mingyu; Ma, Li; Shao, Ming'an; Wei, Xiaorong; Jia, Yuhua; Sun, Shuchen et al. (2021):
843   Chinese zokor (Myospalax fontanierii) excavating activities lessen runoff but facilitate soil
844   erosion – A simulation experiment. In: *CATENA* 202 (8), S. 105248. DOI:
845   10.1016/j.catena.2021.105248.
846 Coombes, Martin A. (2016): Biogeomorphology: diverse, integrative and useful. In: *Earth Surf.*
847   *Process. Landforms* 41 (15), S. 2296–2300. DOI: 10.1002/esp.4055.
848 Corenblit, Dov; Corbara, Bruno; Steiger, Johannes (2021): Biogeomorphological eco-evolutionary
849   feedback between life and geomorphology: a theoretical framework using fossorial mammals.
850   In: *Die Naturwissenschaften* 108 (6), S. 55. DOI: 10.1007/s00114-021-01760-y.
851 Eccard, Jana A.; Herde, Antje (2013): Seasonal variation in the behaviour of a short-lived rodent.
852   In: *BMC ecology* 13, S. 43. DOI: 10.1186/1472-6785-13-43.
853 Eitel, Jan U.H.; Williams, C. Jason; Vierling, Lee A.; Al-Hamdan, Osama Z.; Pierson, Frederick B.
854   (2011): Suitability of terrestrial laser scanning for studying surface roughness effects on
855   concentrated flow erosion processes in rangelands. In: *CATENA* 87 (3), S. 398–407. DOI:
856   10.1016/j.catena.2011.07.009.
857 Eltner, A.; Mulsow, C.; Maas, H.-G. (2013): QUANTITATIVE MEASUREMENT OF SOIL
858   EROSION FROM TLS AND UAV DATA. In: *Int. Arch. Photogramm. Remote Sens. Spatial Inf.*
859   *Sci.* XL-1/W2, S. 119–124. DOI: 10.5194/isprsarchives-XL-1-W2-119-2013.
860 Eltner, A.; Schneider, D.; Maas, H.-G. (2016a): INTEGRATED PROCESSING OF HIGH
861   RESOLUTION TOPOGRAPHIC DATA FOR SOIL EROSION ASSESSMENT

CONSIDERING DATA ACQUISITION SCHEMES AND SURFACE PROPERTIES. In: *Int. Arch. Photogramm. Remote Sens. Spatial Inf. Sci.* XLI-B5, S. 813–819. DOI: 10.5194/isprsarchives-XLI-B5-813-2016.

Eltner, Anette; Kaiser, Andreas; Abellan, Antonio; Schindewolf, Marcus (2017): Time lapse structure-from-motion photogrammetry for continuous geomorphic monitoring. In: *Earth Surf. Process. Landforms* 42 (14), S. 2240–2253. DOI: 10.1002/esp.4178.

Eltner, Anette; Kaiser, Andreas; Castillo, Carlos; Rock, Gilles; Neugirg, Fabian; Abellán, Antonio (2016b): Image-based surface reconstruction in geomorphometry – merits, limits and developments. In: *Earth Surf. Dynam.* 4 (2), S. 359–389. DOI: 10.5194/esurf-4-359-2016.

Gabet, Emmanuel J.; Reichman, O. J.; Seabloom, Eric W. (2003): The Effects of Bioturbation on Soil Processes and Sediment Transport. In: *Annu. Rev. Earth Planet. Sci.* 31 (1), S. 249–273. DOI: 10.1146/annurev.earth.31.100901.141314.

Galland, Olivier; Bertelsen, Håvard S.; Guldstrand, Frank; Girod, Luc; Johannessen, Rikke F.; Bjugger, Fanny et al. (2016): Application of open-source photogrammetric software MicMac for monitoring surface deformation in laboratory models. In: *J. Geophys. Res. Solid Earth* 121 (4), S. 2852–2872. DOI: 10.1002/2015JB012564.

Garreaud, RenéD.; Rutllant, JoséA.; Fuenzalida, Humberto (2002): Coastal Lows along the Subtropical West Coast of South America: Mean Structure and Evolution. In: *Mon. Wea. Rev.* 130 (1), S. 75–88. DOI: 10.1175/1520-0493(2002)130<0075:CLATSW>2.0.CO;2.

Grigusova, Paulina; Larsen, Annegret; Achilles, Sebastian; Klug, Alexander; Fischer, Robin; Kraus, Diana et al. (2021): Area-Wide Prediction of Vertebrate and Invertebrate Hole Density and Depth across a Climate Gradient in Chile Based on UAV and Machine Learning. In: *Drones* 5 (3), S. 86. DOI: 10.3390/drones5030086.

Hakonson, T. E. (1999): The Effects of Pocket Gopher Burrowing on Water Balance and Erosion from Landfill Covers. In: *J. environ. qual.* 28 (2), S. 659–665. DOI: 10.2134/jeq1999.00472425002800020033x.

Hall, Kevin; Boelhouwers, Jan; Driscoll, Kevin (1999): Animals as Erosion Agents in the Alpine Zone: Some Data and Observations from Canada, Lesotho, and Tibet. In: *Arctic, Antarctic, and Alpine Research* 31 (4), S. 436–446. DOI: 10.1080/15230430.1999.12003328.

Hancock, Greg; Lowry, John (2021): Quantifying the influence of rainfall, vegetation and animals on soil erosion and hillslope connectivity in the monsoonal tropics of northern Australia. In: *Earth Surf. Process. Landforms* 46 (10), S. 2110–2123. DOI: 10.1002/esp.5147.

Hänsel, Phoebe; Schindewolf, Marcus; Eltner, Anette; Kaiser, Andreas; Schmidt, Jürgen (2016): Feasibility of High-Resolution Soil Erosion Measurements by Means of Rainfall Simulations and SfM Photogrammetry. In: *Hydrology* 3 (4), S. 38. DOI: 10.3390/hydrology3040038.

Hazelhoff, L.; van Hoof, P.; Imeson, A. C.; Kwaad, F. J. P. M. (1981): The exposure of forest soil to erosion by earthworms. In: *Earth Surf. Process. Landforms* 6 (3-4), S. 235–250. DOI: 10.1002/esp.3290060305.

Herbst, M.; Bennett, N. C. (2006): Burrow architecture and burrowing dynamics of the endangered Namaqua dune mole rat (Bathyergus janetta) (Rodentia: Bathyergidae). In: *Journal of Zoology* 270 (3), S. 420–428. DOI: 10.1111/j.1469-7998.2006.00151.x.

Horn, B.K.P. (1981): Hill shading and the reflectance map. In: *Proc. IEEE* 69 (1), S. 14–47. DOI: 10.1109/PROC.1981.11918.

Imeson, A. C. (1977): Splash erosion, animal activity and sediment supply in a small forested Luxembourg catchment. In: *Earth Surf. Process. Landforms* 2 (2-3), S. 153–160. DOI: 10.1002/esp.3290020207.

Imeson, A. C.; Kwaad, F. J. P. M. (1976): Some Effects of Burrowing Animals on Slope Processes in the Luxembourg Ardennes. In: *Geografiska Annaler: Series A, Physical Geography* 58 (4), S. 317–328. DOI: 10.1080/04353676.1976.11879941.

Iserloh, T.; Ries, J. B.; Arnáez, J.; Boix-Fayos, C.; Butzen, V.; Cerdà, A. et al. (2013): European small portable rainfall simulators: A comparison of rainfall characteristics. In: *CATENA* 110 (2), S. 100–112. DOI: 10.1016/j.catena.2013.05.013.

914 James, M. R.; Robson, S. (2014): Sequential digital elevation models of active lava flows from
915   ground-based stereo time-lapse imagery. In: *ISPRS Journal of Photogrammetry and Remote*
916   *Sensing* 97 (3), S. 160–170. DOI: 10.1016/j.isprsjprs.2014.08.011.
917 Jimenez, J. E.; Feinsinger, P.; Jaksi, F. M. (1992): Spatiotemporal Patterns of an Irruption and
918   Decline of Small Mammals in Northcentral Chile. In: *Journal of Mammalogy* 73 (2), S. 356–
919   364. DOI: 10.2307/1382070.
920 Jones, Clive G.; Gutiérrez, Jorge L.; Byers, James E.; Crooks, Jeffrey A.; Lambrinos, John G.;
921   Talley, Theresa S. (2010): A framework for understanding physical ecosystem engineering by
922   organisms. In: *Oikos* 119 (12), S. 1862–1869. DOI: 10.1111/j.1600-0706.2010.18782.x.
923 Kaiser, Andreas; Neugirg, Fabian; Rock, Gilles; Müller, Christoph; Haas, Florian; Ries, Johannes;
924   Schmidt, Jürgen (2014): Small-Scale Surface Reconstruction and Volume Calculation of Soil
925   Erosion in Complex Moroccan Gully Morphology Using Structure from Motion. In: *Remote*
926   *Sensing* 6 (8), S. 7050–7080. DOI: 10.3390/rs6087050.
927 Katzman, Elena A.; Zaytseva, Elena A.; Feoktistova, Natalia Yu.; Tovpinetz, Nikolay N.;
928   Bogomolov, Pavel L.; Potashnikova, Ekaterina V.; Surov, Alexey V. (2018): Seasonal Changes
929   in Burrowing of the Common Hamster (Cricetus cricetus L., 1758) (Rodentia: Cricetidae) in the
930   City. In: *PJE* 17 (3), S. 251–258. DOI: 10.18500/1684-7318-2018-3-251-258.
931 Kinlaw, A.; Grasmueck, M. (2012): Evidence for and geomorphologic consequences of a reptilian
932   ecosystem engineer: The burrowing cascade initiated by the Gopher Tortoise. In:
933   *Geomorphology* 157-158 (4), S. 108–121. DOI: 10.1016/j.geomorph.2011.06.030.
934 Kromer, Ryan; Walton, Gabe; Gray, Brian; Lato, Matt; Group, Robert (2019): Development and
935   Optimization of an Automated Fixed-Location Time Lapse Photogrammetric Rock Slope
936   Monitoring System. In: *Remote Sensing* 11 (16), S. 1890. DOI: 10.3390/rs11161890.
937 Kukko, Antero; Hyyppä, Juha (2009): Small-footprint Laser Scanning Simulator for System
938   Validation, Error Assessment, and Algorithm Development. In: *photogramm eng remote sensing*
939   75 (10), S. 1177–1189. DOI: 10.14358/PERS.75.10.1177.
940 Larsen, A.; Nardin, W.; Lageweg, W. I.; Bätz, N. (2021): Biogeomorphology, quo vadis? On
941   processes, time, and space in biogeomorphology. In: *Earth Surf. Process. Landforms* 46 (1), S.
942   12–23. DOI: 10.1002/esp.5016.
943 Le Hir, P.; Monbet, Y.; Orvain, F. (2007): Sediment erodability in sediment transport modelling:
944   Can we account for biota effects? In: *Continental Shelf Research* 27 (8), S. 1116–1142. DOI:
945   10.1016/j.csr.2005.11.016.
946 Lehnert, Lukas W.; Thies, Boris; Trachte, Katja; Achilles, Sebastian; Osses, Pablo; Baumann, Karen
947   et al. (2018): A Case Study on Fog/Low Stratus Occurrence at Las Lomitas, Atacama Desert
948   (Chile) as a Water Source for Biological Soil Crusts. In: *Aerosol Air Qual. Res.* 18 (1), S. 254–
949   269. DOI: 10.4209/aaqr.2017.01.0021.
950 Li, Guorong; Li, Xilai; Li, Jinfang; Chen, Wenting; Zhu, Haili; Zhao, Jianyun; Hu, Xiasong
951   (2019a): Influences of Plateau Zokor Burrowing on Soil Erosion and Nutrient Loss in Alpine
952   Meadows in the Yellow River Source Zone of West China. In: *Water* 11 (11), S. 2258. DOI:
953   10.3390/w11112258.
954 Li, Larry (2014): Time-of-Flight Camera – An Introduction. Technical White Paper. Hg. v. Texas
955   Instruments. Online verfügbar unter https://www.ti.com/lit/wp/sloa190b/sloa190b.pdf, zuletzt
956   geprüft am 22.12.2021.
957 Li, T. C.; Shao, M. A.; Jia, Y. H.; Jia, X. X.; Huang, L. M.; Gan, M. (2019b): Small‐scale
958   observation on the effects of burrowing activities of ants on soil hydraulic processes. In: *Eur J*
959   *Soil Sci* 70 (2), S. 236–244. DOI: 10.1111/ejss.12748.
960 Li, Tongchuan; Jia, Yuhua; Shao, Ming'an; Shen, Nan (2019c): Camponotus japonicus burrowing
961   activities exacerbate soil erosion on bare slopes. In: *Geoderma* 348 (4), S. 158–167. DOI:
962   10.1016/j.geoderma.2019.04.035.
963 Li, Tongchuan; Shao, Ming'an; Jia, Yuhua; Jia, Xiaoxu; Huang, Laiming (2018): Small-scale
964   observation on the effects of the burrowing activities of mole crickets on soil erosion and
965   hydrologic processes. In: *Agriculture, Ecosystems & Environment* 261 (4), S. 136–143. DOI:

966   10.1016/j.agee.2018.04.010.

967 Longoni, Laura; Papini, Monica; Brambilla, Davide; Barazzetti, Luigi; Roncoroni, Fabio; Scaioni,
968   Marco; Ivanov, Vladislav (2016): Monitoring Riverbank Erosion in Mountain Catchments Using
969   Terrestrial Laser Scanning. In: *Remote Sensing* 8 (3), S. 241. DOI: 10.3390/rs8030241.

970 Malizia, Ana I. (1998): Population dynamics of the fossorial rodent Ctenomys talarum (Rodentia:
971   Octodontidae). In: *Journal of Zoology* 244 (4), S. 545–551. DOI: 10.1111/j.1469-
972   7998.1998.tb00059.x.

973 MALLALIEU, JOSEPH; CARRIVICK, JONATHAN L.; QUINCEY, DUNCAN J.; SMITH,
974   MARK W.; JAMES, WILLIAM H.M. (2017): An integrated Structure-from-Motion and time-
975   lapse technique for quantifying ice-margin dynamics. In: *J. Glaciol.* 63 (242), S. 937–949. DOI:
976   10.1017/jog.2017.48.

977 Meysman, Filip J. R.; Boudreau, Bernard P.; Middelburg, Jack J. (2003): Relations between local,
978   nonlocal, discrete and continuous models of bioturbation. In: *Journal of Marine Research* 61
979   (3), S. 391–410. DOI: 10.1357/002224003322201241.

980 Monteverde, Martín J.; Piudo, Luciana (2011): Activity Patterns of the Culpeo Fox (Lycalopex
981   Culpaeus Magellanica) in a Non-Hunting Area of Northwestern Patagonia, Argentina. In:
982   *Mammal Study* 36 (3), S. 119–125. DOI: 10.3106/041.036.0301.

983 Morris, Rowena H.; Buckman, Solomon; Connelly, Paul; Dragovich, Deirdre; Ostendorf, Bertram;
984   and Bradstock, Ross A. (2011): The dirt on assessing post-fire erosion in the Mount Lofty
985   Ranges: comparing methods.

986 Nasermoaddeli, M. B.; Pasche, E. (2008): Application of terrestrial 3D scanner in quantification of
987   the riverbank erosion and deposition. Institute of river and coastal engineering, Technical
988   university Hamburg-Harburg, Hamburg,. Online verfügbar unter
989   https://www.tuhh.de/t3resources/wb/Publikationen/MA-
990   Veroeffentlichungen/nasermoaddelli/riverflow2008.pdf, zuletzt geprüft am 22.12.2021.

991 Pang, Xiao Pan; Guo, Zheng Gang (2017): Plateau pika disturbances alter plant productivity and
992   soil nutrients in alpine meadows of the Qinghai-Tibetan Plateau, China. In: *Rangel. J.* 39 (2), S.
993   133. DOI: 10.1071/RJ16093.

994 Reichman, O. J.; Seabloom, Eric W. (2002): The role of pocket gophers as subterranean ecosystem
995   engineers. In: *Trends in Ecology & Evolution* 17 (1), S. 44–49. DOI: 10.1016/S0169-
996   5347(01)02329-1.

997 Richards, Paul J.; Humphreys, Geoff S. (2010): Burial and turbulent transport by bioturbation: a 27-
998   year experiment in southeast Australia. In: *Earth Surf. Process. Landforms* 21 (2), n/a-n/a. DOI:
999   10.1002/esp.2007.

1000 Ridd, Peter V. (1996): Flow Through Animal Burrows in Mangrove Creeks. In: *Estuarine, Coastal
1001   and Shelf Science* 43 (5), S. 617–625. DOI: 10.1006/ecss.1996.0091.

1002 Romañach, Stephanie S.; Reichman, O. J.; Seabloom, E. W. (2005): Seasonal influences on
1003   burrowing activity of a subterranean rodent, Thomomys bottae. In: *Journal of Zoology* 266 (3),
1004   S. 319–325. DOI: 10.1017/S0952836905006941.

1005 Rutin, J. (1996): The burrowing activity of scorpions (Scorpio maurus palmatus) and their potential
1006   contribution to the erosion of Hamra soils in Karkur, central Israel. In: *Geomorphology* 15 (2),
1007   S. 159–168. DOI: 10.1016/0169-555X(95)00120-T.

1008 Sarbolandi, Hamed; Plack, Markus; Kolb, Andreas (2018): Pulse Based Time-of-Flight Range
1009   Sensing. In: *Sensors (Basel, Switzerland)* 18 (6). DOI: 10.3390/s18061679.

1010 Schiffers, Katja; Teal, Lorna Rachel; Travis, Justin Mark John; Solan, Martin (2011): An open
1011   source simulation model for soil and sediment bioturbation. In: *PloS one* 6 (12), e28028. DOI:
1012   10.1371/journal.pone.0028028.

1013 Sharon, David (1980): The distribution of hydrologically effective rainfall incident on sloping
1014   ground. In: *Journal of Hydrology* 46 (1-2), S. 165–188. DOI: 10.1016/0022-1694(80)90041-4.

1015 Thomsen, L. M.; Baartman, J. E. M.; Barneveld, R. J.; Starkloff, T.; Stolte, J. (2015): Soil surface
1016   roughness: comparing old and new measuring methods and application in a soil erosion model.
1017   In: *SOIL* 1 (1), S. 399–410. DOI: 10.5194/soil-1-399-2015.

1018 Übernickel, Kirstin; Ehlers, Todd A.; Paulino, Leandro; Fuentes Espoz, Juan-Pablo (2021a): Time
1019   series of meteorological stations on an elevational gradient in National Park La Campana, Chile.
1020   Unter Mitarbeit von Kirstin Übernickel, Todd A. Ehlers, Leandro Paulino, Juan-Pablo Fuentes
1021   Espoz, Ramiro Bernales-Noguera, Willi Kappler et al.
1022 Übernickel, Kirstin; Pizarro-Araya, Jaime; Bhagavathula, Susila; Paulino, Leandro; Ehlers, Todd A.
1023   (2021b): Reviews and syntheses: Composition and characteristics of burrowing animals along a
1024   climate and ecological gradient, Chile. In: *Biogeosciences* 18 (20), S. 5573–5594. DOI:
1025   10.5194/bg-18-5573-2021.
1026 Valdés-Pineda, Rodrigo; Valdés, Juan B.; Diaz, Henry F.; Pizarro-Tapia, Roberto (2016): Analysis
1027   of spatio-temporal changes in annual and seasonal precipitation variability in South America-
1028   Chile and related ocean-atmosphere circulation patterns. In: *Int. J. Climatol.* 36 (8), S. 2979–
1029   3001. DOI: 10.1002/joc.4532.
1030 Voiculescu, Mircea; Ianăş, Ana-Neli; Germain, Daniel (2019): Exploring the impact of snow vole
1031   (Chionomys nivalis) burrowing activity in the Făgăraş Mountains, Southern Carpathians
1032   (Romania): Geomorphic characteristics and sediment budget. In: *CATENA* 181 (1), S. 104070.
1033   DOI: 10.1016/j.catena.2019.05.016.
1034 Wei, Xinghu; Li, Sen; Yang, Ping; Cheng, Huaishun (2007): Soil erosion and vegetation succession
1035   in alpine Kobresia steppe meadow caused by plateau pika—A case study of Nagqu County,
1036   Tibet. In: *Chin. Geograph.Sc.* 17 (1), S. 75–81. DOI: 10.1007/s11769-007-0075-0.
1037 Wilcox, Andrew C.; Escauriaza, Cristian; Agredano, Roberto; Mignot, Emmanuel; Zuazo, Vicente;
1038   Otárola, Sebastián et al. (2016): An integrated analysis of the March 2015 Atacama floods. In:
1039   *Geophys. Res. Lett.* 43 (15), S. 8035–8043. DOI: 10.1002/2016GL069751.
1040 Wilkinson, Marshall T.; Richards, Paul J.; Humphreys, Geoff S. (2009): Breaking ground:
1041   Pedological, geological, and ecological implications of soil bioturbation. In: *Earth-Science
1042   Reviews* 97 (1-4), S. 257–272. DOI: 10.1016/j.earscirev.2009.09.005.
1043 Yair, A. (1995): Short and long term effects of bioturbation on soil erosion, water resources and soil
1044   development in an arid environment. In: *Geomorphology* 13 (1-4), S. 87–99. DOI:
1045   10.1016/0169-555X(95)00025-Z.
1046 Yáñez, E.; Barbieri, M.A; Silva, C.; Nieto, K.; Espíndola, F. (2001): Climate variability and pelagic
1047   fisheries in northern Chile. In: *Progress in Oceanography* 49 (1-4), S. 581–596. DOI:
1048   10.1016/S0079-6611(01)00042-8.
1049 Yoo, Kyungsoo; Amundson, Ronald; Heimsath, Arjun M.; Dietrich, William E. (2005): Process-
1050   based model linking pocket gopher (Thomomys bottae) activity to sediment transport and soil
1051   thickness. In: *Earth Surf. Process. Landforms* 33 (11), S. 917. DOI: 10.1130/G21831.1.
1052
1053